Department of Physics and Astronomy
Heidelberg University

Master Thesis in Physics
submitted by

Claudia Volk

born in Balingen (Germany)

2023

Pound-Drever-Hall Locking an Infrared Fibre Laser to a High-Finesse ULE Cavity

This Master Thesis has been carried out by Claudia Volk at the
Max-Planck-Institut für Kernphysik in Heidelberg
under the supervision of
Prof. Dr. José Ramón Crespo López-Urrutia

Pound-Drever-Hall Locking an Infrared Fibre Laser to a High-Finesse ULE Cavity:

This thesis presents the implementation of the Pound-Drever-Hall (PDH) locking technique for stabilising a laser to a high-finesse optical reference cavity. The ultimate goal is to realise a stable and accurate frequency reference for high-precision spectroscopy experiments on highly charged ions in a superconducting Paul trap. This work details the construction of a housing for the ultra-low expansion glass (ULE) resonator, as well as the analysis of different intensity signals during the incoupling process and the initial PDH operation. First successful locking was achieved, although with limited stability, possibly due to insufficient feedback bandwidth or operating the cavity in air at the current time. External perturbations such as temperature and pressure fluctuations that could lead to the current instability and noise level were identified and work is ongoing to improve these aspects, including by operating the cavity in vacuum for which the housing is already prepared.

Pound-Drever-Hall-Kopplung eines Infrarot-Faserlasers an eine ULE-Kavität hoher Finesse:

In dieser Masterarbeit wird die Implementierung der Pound-Drever-Hall (PDH) Locking-Methode zur Stabilisierung eines Lasers an einer optischen Referenzkavität hoher Finesse vorgestellt. Ziel ist es, eine stabile und genaue Frequenzreferenz für hochpräzise Spektroskopieexperimente an hochgeladenen Ionen in einer supraleitenden Paul-Falle zu realisieren. Im Verlauf dieser Arbeit werden die Konstruktion eines Gehäuses für den Glasresonator (Ultra Low Expansion Glass, ULE), sowie die Analyse verschiedener Intensitätssignale während des Einkopplungsprozesses und des ersten PDH-Betriebs beschrieben. Eine erste erfolgreiche Feedback-Kopplung wurde umgesetzt, wenn auch mit eingeschränkter Stabilität, was möglicherweise auf eine unzureichende Rückkopplungsbandbreite oder den Betrieb der Kavität in Luft zum gegenwärtigen Zeitpunkt zurückgeführt werden kann. Externe Störeinflüsse wie Temperatur- und Druckfluktuationen, die zu der momentanen Instabilität und dem Rauschpegel führen könnten, wurden identifiziert, und es wird fortlaufend daran gearbeitet, diese Aspekte zu verbessern, auch durch Betrieb der Kavität im Vakuum, wofür das Gehäuse bereits ausgelegt ist.

Contents

1 Introduction

1.1 Ultra-Stable Lasers

The invention and realisation of the laser in 1960 [1] provided a new tool with which light could be generated with special properties – light could now be produced with very high spatial and temporal coherence. This had a profound impact on numerous scientific fields and transformed research, technology, and applications. Lasers are at the core of modern optics and photonics research including quantum optics [2] and quantum information processing [3], but they also play a crucial role in atomic and molecular physics [4, 5] and metrology [6]. Furthermore, they have become an essential tool in other scientific disciplines such as astronomy [7] and biology [8], as well as more application-oriented areas such as medicine [9] and communications [10].

Spectroscopy describes the study of (electromagnetic) spectra resulting from the interaction between matter and radiation. In the beginning, it consisted of investigations of the solar spectrum [11] and the emission lines of heated substances [12]. However, with the invention of lasers and the availability of a coherent and monochromatic light source, precise and selective excitation of atomic and molecular systems are made possible. This enables direct measurements of atomic structures, leading for instance to the development of laser cooling [13].

Laser light can have some specialised properties, for instance it can be made to have extremely high intensities with amplification and beam focusing. The light can also be pulsed instead of supplying a constant intensity, which can be made as short as tens of attoseconds [14]. Furthermore, pulsed lasers with specific phase relations can exhibit an interesting pattern in their frequency spectrum. The equidistant peaks of the so called frequency comb [15, 16] make direct and precise measurements of optical frequencies possible.

Optical interferometry, exemplified by the Michelson interferometer [17], was also transformed into a new tool of physics by the introduction of the laser. More types of interferometers have emerged since then, and have proven to be a reliable method for characterising and controlling laser light. The most notable and direct application of laser interferometry is the detection of gravitational waves [18].

A widely used component in setups to stabilize lasers is the Fabry-Pérot interferometer. Ultra-stable lasers are essential for optical atomic clocks [19] and provide an important tool for precision tests of fundamental physics [20, 21]. A stabilised laser with a linewidth

of less than 1 Hz was reached in 1999 [22]. The research to develop more stable laser setups continuously progresses, with cryogenic reference cavities to reduce thermal noise or longer glass cavities to reduce thermal effects on the fractional frequency stability. In 2012, a fractional frequency instability of 10^{-16} at short timescales has been achieved with a cryogenic setup [23].

1.2 Highly Charged Ions

An atomic system refers to an arrangement of a single nucleus that is surrounded by a number of electrons. This includes neutral atoms with equal charge in the nucleus as in the surrounding electrons, as well as charged ions where the number of electrons around the same nucleon has changed. Every chemical element has at least as many different charge states as it does electrons – focusing mainly on positively charged ions – many of them highly charged with a large positive total charge. These highly charged ions (HCIs) therefore make up largest fraction of possible atomic systems and, although they are rare on earth, they amount to a large portion of the visible matter in the universe. Their outer electrons are strongly bound to the nucleus and because many of the atomic properties scale with the nuclear charge, they behave differently than their less charged counterparts [24]. However, for most HCIs, many of their atomic transitions remain to be discovered or measured accurately (this gap of knowledge has also been called the 'sea of ignorance' [25]).

Several HCI species have energy levels and transitions that show a high sensitivity to the variation of the fine-structure constant $\dot{\alpha}/\alpha$ [26] or possible fifth force mediators [27], making them interesting to fundamental research. Additionally, due to the strong binding of the remaining electrons to the highly positively charged nucleus, the ion's energy levels are a lot less susceptible to external perturbations like Stark shifts. This makes them useful for precision experiments where these outside influences have to be kept small and well controlled. HCIs have been proposed as good optical clock candidates – the first such clock has been realised in 2022 [28] – as well as good probe for new physics for the aforementioned reasons [29].

To reach the precision necessary for these kinds of spectroscopic measurements, the HCIs have to be cooled down to reduce motion-induced broadening of the transitions. They are typically produced at high temperatures, e.g. inside an electron beam ion trap (EBIT) where the ions remain in a gas cloud and constant collisions lead to temperatures of hundreds of thousands or even millions of degrees Celsius [30]. Direct laser cooling of HCIs is not possible due to the necessary fast-cycling electric-dipole (E1) transitions being shifted to far shorter wavelengths into the X-ray regime where no laser sources exist.

1.3 The Cryogenic Paul Trap Experiment

The cryogenic Paul trap experiment (CryPTEx) at the Max-Planck-Institut für Kernphysik in Heidelberg is designed to simultaneously trap HCIs and singly charged beryllium ions [31]. The heart of the currently operating second iteration CryPTEx-II is made up of a superconducting resonator that acts as a linear Paul trap [32, 33]. The goal is to perform quantum logic spectroscopy [34] on a HCI trapped together with a single beryllium ion.

The HCIs are produced in a Heidelberg compact EBIT [35] from which they extracted and re-trapped in the cryogenic Paul trap. There, they form a Coulomb crystal with laser cooled singly charged beryllium ions [36]. Since the HCIs share motional states in the Paul trap with the beryllium ions, they are sympathetically cooled as well. This includes Doppler cooling, along with ground-state cooling via Raman sideband cooling.

Once a Coulomb crystal of one HCI and one beryllium ion is cooled to the motional ground state, one can apply quantum logic to perform spectroscopy. As in other types of laser spectroscopy, the precision with which a transition frequency can be measured is limited by the precision of the laser used to interrogate this transition.

A system of spectroscopy lasers and a frequency comb is ready to be implemented into the setup. The goal is to expand the setup to include a stabilised reference laser to increase the precision of the spectroscopic measurements.

2 Theory

This chapter will provide the relevant theoretical background for describing the locking of a laser to a stable optical cavity. It will cover the description of light as a beam in section 2.1 and the theory of optical resonators and the Pound-Drever-Hall technique in section 2.2.

2.1 Beam Optics

The behaviour of light in simple optical setups can often be explained using ray optics, where light is described with rays that follow simple geometrical rules. Each medium has a refractive index n indicating the change from the speed of light in vacuum c (where $n = 1$). The time it takes the light ray to travel a certain path is the optical path length and Fermat's principle states that the light will travel the path where this is minimal. Effects of the electromagnetic field and of the wavelength are neglected. The failure of this approach is already evident in experiments such as the single or double slit, where things like interference phenomena have to be considered. To describe these things, including many more e.g. laser cavities, one needs to at the very least consider light as a wave. The following discussion of wave and beam optics is mainly based on ref. [37].

In wave optics, light is treated as a real scalar wavefunction $u(\boldsymbol{r}, t)$, depending on the position $\boldsymbol{r} = (x, y, z)$ in space and time t. The wavefunction is a solution to the scalar wave equation

$$\frac{1}{c^2}\frac{\partial^2}{\partial t^2}u - \Delta u = 0\,, \tag{2.1}$$

where $\Delta = \partial_x^2 + \partial_y^2 + \partial_z^2$ is the Laplace operator.

Often, a complex representation is used where u is the real part of a complex wavefunction $U(\boldsymbol{r}, t)$ which allows for an easier description of the phase and amplitude in a single quantity.

We will start by considering monochromatic waves where the time dependence is harmonic with a singular frequency f[1] at every point in space. This allows for a factor of $\exp(i2\pi ft)$

[1] For (near-)optical lightwaves one typically considers frequencies in the range of $3 \cdot 10^{11}$ Hz to $3 \cdot 10^{16}$ Hz.

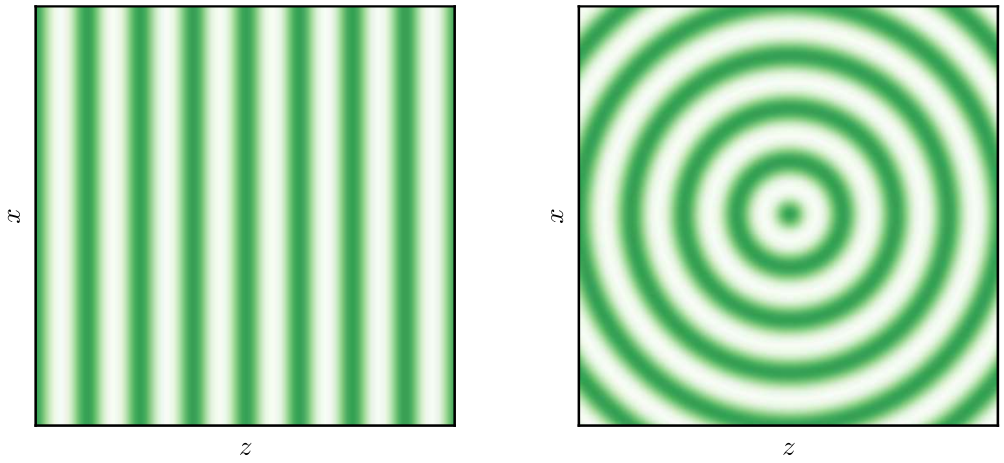

(a) **(b)**

Figure 2.1: Wavefronts are the planes of constant phase of a wave in 3-dimensional space. In this figure, we see the wavefronts in x and z of two different types of fundamental waves. **(a)** This picture shows the wavefronts of an ideal plane wave propagating in z direction. The wavefronts have no curvature – or rather a radius of infinity – and therefore, the propagation direction which is perpendicular to the wavefronts is the same at every point. **(b)** Here, we can see the wavefronts of a spherical wave originating at the centre. As the name suggests, the wavefronts are spheres around the origin which have linearly increasing radii of curvature. From its origin, this wave propagates in all spatial directions at the same time and can therefore be described as maximally divergent.

to be separated from the general complex wavefunction, leaving a complex amplitude that includes the amplitude and the phase which will only depend on position:

$$U(\boldsymbol{r}, t) = U(\boldsymbol{r}) e^{i2\pi f t} \tag{2.2}$$

Separating the spatial part – the complex amplitude $U(\boldsymbol{r})$ – and the time-dependent part in this way allows for the wave equation (2.1) to be converted into a time-independent equation, the Helmholtz equation:

$$\Delta U + k^2 U = 0\,. \tag{2.3}$$

Planes where the phase of the wavefunction is constant – or rather a multiple m of 2π ($\phi(\boldsymbol{r}) = m\,2\pi$) – are called wavefronts. Some fundamental solutions to the Helmholtz equation are plane and spherical waves, both named after the shape of their respective wavefronts, which can be seen in figure 2.1.

They also illustrate the main problem when it comes to light transfer through free space, of how to represent directed but focused laser beams. Plane waves have a well-defined direction of propagation and do not diverge, but their expansion is infinite with constant

intensity throughout – not physically feasible. Circular waves are spatially confined in the way that the intensity peaks at the origin, yet they radiate out in all directions isotropically and can therefore be described as infinitely divergent.

2.1.1 The Gaussian Beam

To realise and describe waves in a form where they have both a clear direction of propagation and a limited spatial spread perpendicular to it, it is convenient to introduce the concept of paraxial waves. Starting with a plane wave in z direction with wavevector $k = 2\pi/\lambda$, we modulate its amplitude with slow-varying envelope $A(\boldsymbol{r})$ such that locally it can still be treated like a plane wave.

$$U(\boldsymbol{r}) = A(\boldsymbol{r})e^{-ikz} \tag{2.4}$$

This envelope $A(\boldsymbol{r})$ has to satisfy the paraxial Helmholtz equation:

$$\nabla_T^2 A - i\,2k\frac{\partial A}{\partial z} = 0\,. \tag{2.5}$$

Here, $\nabla_T^2 = \partial_x^2 + \partial_y^2$ is the transversal Laplace operator. Equation (2.5) is derived from the Helmholtz equation (2.3), where the second derivative of A with respect to z is neglected due to the slow-varying nature of the envelope.

A solution to this equation is the Gaussian beam, which has the properties we are looking for. It has a clear direction – with wavefronts that vary mainly along this path – and a small angular dispersion with most of the power concentrated along the beam axis. The solution can be derived via the paraboloidal wave, its complex amplitude is

$$U(\boldsymbol{r}) = \frac{A_1}{z}\exp[-ikz]\exp\left[-ik\frac{x^2+y^2}{2z}\right]\,, \tag{2.6}$$

where A_1 is a constant. This has the slow-varying envelope

$$A(\boldsymbol{r}) = \frac{A_1}{z}\exp\left[-ik\frac{x^2+y^2}{2z}\right]\,, \tag{2.7}$$

which satisfies the paraxial Helmholtz equation.

The complex envelope of the Gaussian beam is obtained from equation (2.7) by replacing z with the so called q-factor $q(z) = z + iz_0$:

$$A(\boldsymbol{r}) = \frac{A_1}{z+iz_0}\exp\left[-ik\frac{x^2+y^2}{2(z+iz_0)}\right]\,. \tag{2.8}$$

The parameter z_0 that is introduced in this definition will be called the Rayleigh range or Rayleigh length. To separate this envelope into its real (amplitude) and imaginary (phase) part, one rewrites the complex q-factor of the Gaussian beam as

$$\begin{aligned}\frac{1}{q(z)} = \frac{1}{z + iz_0} &= \frac{z}{z^2 + z_0^2} - i\,\frac{z_0}{z^2 + z_0^2} \\ &= \frac{1}{z\left(1 + (z_0/z)^2\right)} - i\,\frac{1}{z_0\left(1 + (z/z_0)^2\right)} \\ &=: \frac{1}{R(z)} - i\,\frac{\lambda}{\pi w^2(z)}\,,\end{aligned} \tag{2.9}$$

where the two functions $R(z)$ and $w(z)$ are defined as

$$R(z) = z\left(1 + \left(\frac{z_0}{z}\right)^2\right), \tag{2.10}$$

$$w(z) = \sqrt{\frac{\lambda z_0}{\pi}}\sqrt{1 + \left(\frac{z}{z_0}\right)^2} =: w_0\sqrt{1 + \left(\frac{z}{z_0}\right)^2}. \tag{2.11}$$

It can be shown that $R(z)$ and $w(z)$ are measures of the wavefronts' radius of curvature and the beam width, respectively. The q-factor with its real and imaginary part – sometimes the real and imaginary part of its reciprocal are used instead – fully define a Gaussian beam. It should be noted that here the beam is, without loss of generality, centered around $z = 0$. If necessary, it can be changed to be at position z' by modifying the real part of q with the translation $z \to z - z'$.

Using the functions $R(z)$ and $w(z)$, the envelope can be written as

$$A(\boldsymbol{r}) = A_1 \cdot \left(\frac{1}{R(z)} - i\frac{\lambda}{\pi w^2(z)}\right)\exp\left[-ik\frac{x^2 + y^2}{2R(z)}\right]\exp\left[-\frac{x^2 + y^2}{w^2(z)}\right]. \tag{2.12}$$

After a series of transformations the first term can be rewritten as

$$\begin{aligned}A_1 \cdot \left(\frac{1}{R(z)} - i\frac{\lambda}{\pi w^2(z)}\right) &= A_1\sqrt{\frac{\lambda}{\pi z_0}}\,\frac{-i}{w(z)}\,e^{i\arctan(z/z_0)} \\ &=: A_0\,\frac{w_0}{w(z)}\,e^{i\arctan(z/z_0)}\,,\end{aligned} \tag{2.13}$$

where $A_0 = -iA_1/z_0$ was defined to simplify this formula.

The complex amplitude of a Gaussian beam follows as

$$U(\boldsymbol{r}) = A_0\,\frac{w_0}{w(z)}\exp\left[-\frac{x^2 + y^2}{w^2(z)}\right]\exp\left[-ik\frac{x^2 + y^2}{2R(z)} + i\arctan\left(\frac{z}{z_0}\right) - ikz\right]. \tag{2.14}$$

In the following, some properties of Gaussian beams will be discussed in more detail.

Intensity profile

The beam intensity I follows from the complex amplitude as

$$I(\boldsymbol{r}) = |U(\boldsymbol{r})|^2 \,. \tag{2.15}$$

From equation (2.14), it is clear that the second exponential describing the phase gets cancelled out in the intensity. What is left is a Gaussian function in x- and y-direction with varying amplitude and width along the beam axis.

$$I(\boldsymbol{r}) = |A_0|^2 \left(\frac{w_0}{w(z)}\right)^2 \exp\left[-2\frac{x^2+y^2}{w^2(z)}\right] \tag{2.16}$$

In figure 2.2, the beam profile is pictured for different positions z along the beam.

The peak intensity is always located on the beam axis, but its value changes for different z. In figure 2.3, the behaviour of the maximum intensity $|A_0|^2 \left(w_0/w(z)\right)^2$ is shown.

Integrating the intensity over a plane perpendicular to the beam axis yields the power of the beam at a position z

$$\iint_{\mathbb{R}^2} I(\boldsymbol{r}) dx dy = \frac{1}{2}|A_0|^2 \pi w_0^2 \,. \tag{2.17}$$

As expected from energy conservation, this is independent of z.

Beam width and divergence

The amplitude of the Gaussian beam profile, as well as its width, change along the beam axis z. From equation (2.16) we can see that $w(z)$ corresponds to twice the standard deviation of the Gaussian intensity profile. As a result, the $1/e^2$ width of the intensity at z, where the intensity has decreased by a factor of $1/e^2 \approx 0.135$ compared to the maximum, is $2w(z)$. Therefore, $w(z)$ is also called the beam radius. We have seen its dependence on z in equation (2.11):

$$w(z) = w_0 \sqrt{1 + \left(\frac{z}{z_0}\right)^2} \,. \tag{2.18}$$

The smallest beam width is reached at $z = 0$ where it becomes $2w_0$, this position along the beam axis is called the beam waist. The beam width increases monotonically in each direction, see figure 2.4 . For greater distances $z \gg z_0$ from the beam waist, the divergence becomes linear with the relation

$$w(z) \approx \frac{w_0}{z_0} z \,. \tag{2.19}$$

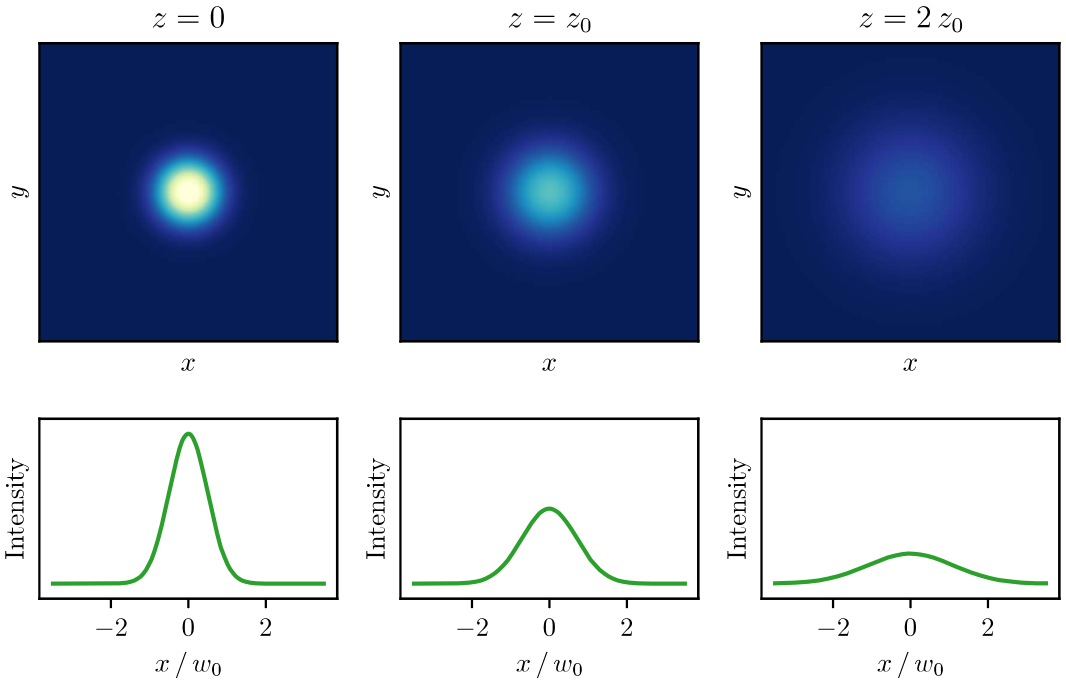

Figure 2.2: Pictured above is the intensity profile of a Gaussian beam at different points along its beam axis. From left to right, the points pictured are $z = 0$, $z = z_0$, and $z = 2z_0$. On the top are the cross section of the beam, and we can observe that the beam becomes wider and weaker further from the origin. On the bottom, we can see the Gaussian profile in x direction (the beam is symmetrical so this also matches the profile in y), where the divergence and the decreasing intensity can be compared more easily.

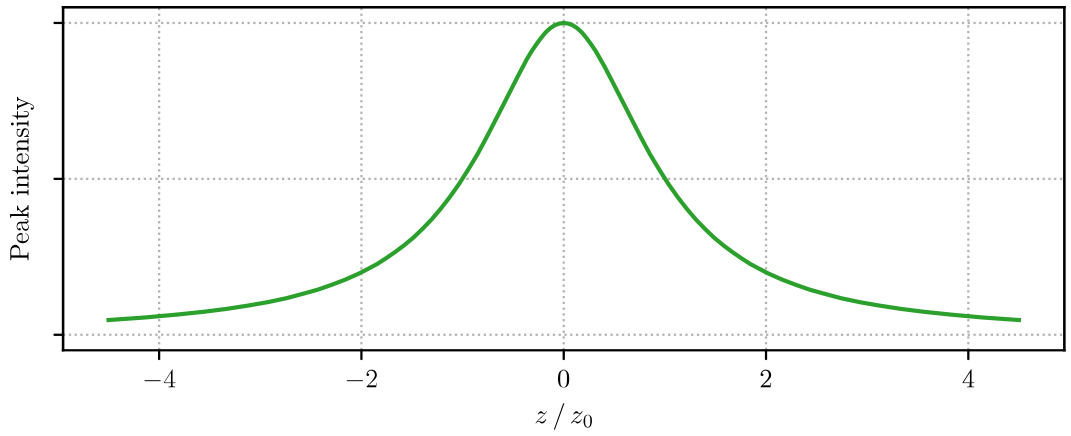

Figure 2.3: Peak intensity of a Gaussian beam along the beam axis – the z-axis. The maximum intensity – in our definition of the Gaussian beam – is always located on this axis. At a distance of z_0 from the origin, the peak intensity of the beam has decreased by a factor of 2.

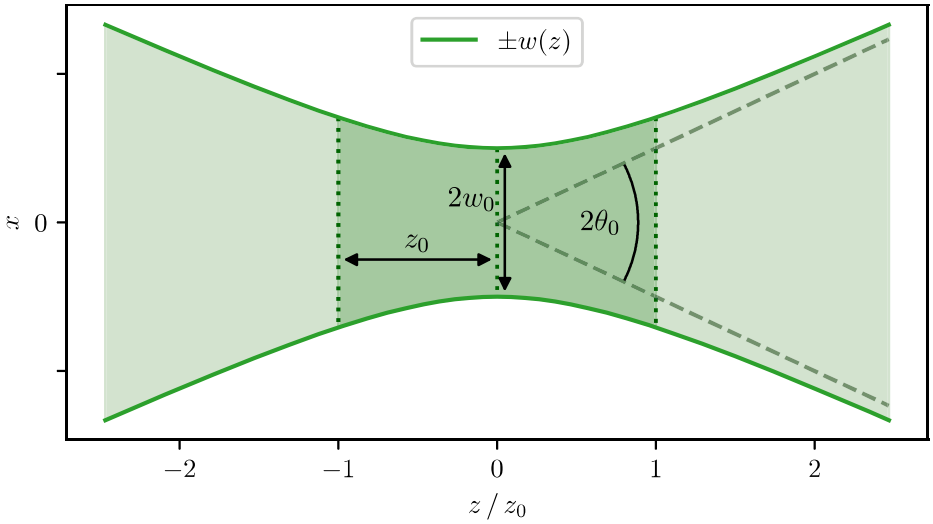

Figure 2.4: The beam diameter $2w(z)$ coincides with the $1/e^2$ width of the Gaussian profile at position z. Therefore, the beam can be and is often visualised in space by this outline, like in the picture above. At the beam waist (the origin), the beam diameter is at its minimum of $2w_0$, while the beam diverges on both sides of the beam waist. Further from the beam waist, the divergence becomes approximately linear with the angle $2\theta_0$. Twice Rayleigh length $2z_0$ is sometimes also called the depth of focus because in this region around the beam waist (shaded darker than the rest of the beam in the picture) the light is the strongest and most focused.

The angle of this divergence is $2\theta_0 \approx 2w_0/z_0$, assuming small angels, and doubled for the total divergence which is symmetrical around the beam axis. It is pictured in figure 2.4 as well.

The parameter w_0, called the waist radius, was defined in equation (2.11) as

$$w_0 = \sqrt{\frac{\lambda z_0}{\pi}}\,, \tag{2.20}$$

and seeing as how w_0 and z_0 relate to each other, the divergence changes with the waist radius as $2\theta_0 \propto 1/w_0$. The smaller the waist radius, the steeper the angle of the divergence. Additionally, a beam with a longer wavelength is more divergent than a beam with the same parameters and a shorter wavelength.

Depth of focus

As seen, the minimum of the beam width is reached at the beam waist at $z = 0$ and increases in both directions along the beam path. One Rayleigh length away from the beam waist, at $z = z_0$, the width has increased by $\sqrt{2}$ and the peak intensity is halved. The area near the beam waist, within z_0 on either side, is the focus of the Gaussian beam and the length $2z_0$, twice the Rayleigh length, is called the depth of focus.

Wavefronts

Going back to the complex amplitude in equation (2.14), before eliminating the parts with the phase information by only looking at the intensity profile, we now have a closer look at the phase of the wave, and at the planes of constant phase – the wavefronts. The phase φ of the Gaussian beam has three contributing terms that we can identify from equation (2.14) as

$$\varphi(\boldsymbol{r}) = kz - \arctan\left(\frac{z}{z_0}\right) + k\,\frac{x^2+y^2}{2R(z)}\,. \tag{2.21}$$

The first term here we can identify as the phase of a simple plane wave, while the other two terms introduce a modification to this.

On the beam axis only the first two terms contribute, and in comparison with a plane wave (that only has a phase of kz), the Gaussian beam is out of phase by up to $\pm\,\pi/2$. This is called the Gouy effect, or the Gouy phase. How this phase retardation changes along the beam can be seen in figure 2.5.

The third term in equation (2.21) introduces a bending to the wavefronts off the beam axis. It can be shown that the function $R(z)$ corresponds closely to the radius of curvature of the wavefronts. The graph of $R(z)$ as well as the wavefronts can be seen in figure 2.5. Around the waist, the behaviour of the wavefronts is close to that of plane waves with the radius of curvature going towards infinity, whereas further along the beam axis they resemble those of a spherical wave.

Beam quality

A Gaussian beam has the lowest divergence possible in free space for a given waist size. To give a simple measure of the quality of a real measured beam, one can therefore compare the product of its measured waist diameter $2w_m$ and divergence $2\theta_m$ to those of a Gaussian beam.

$$M^2 = \frac{2w_m \cdot 2\theta_m}{2w_0 \cdot 2\theta_0} = \frac{2w_m \cdot 2\theta_m}{4\lambda/\pi} \tag{2.22}$$

This is called the M^2-factor. Gaussian beams have the smallest possible divergence for a given waist diameter, hence $M^2 \geq 1$.

It should be noted at this point that this derivation of the Gaussian beam can also be done for electromagnetic optics. Instead of the scalar constants A, one has vectors that represent the electric or magnetic field.

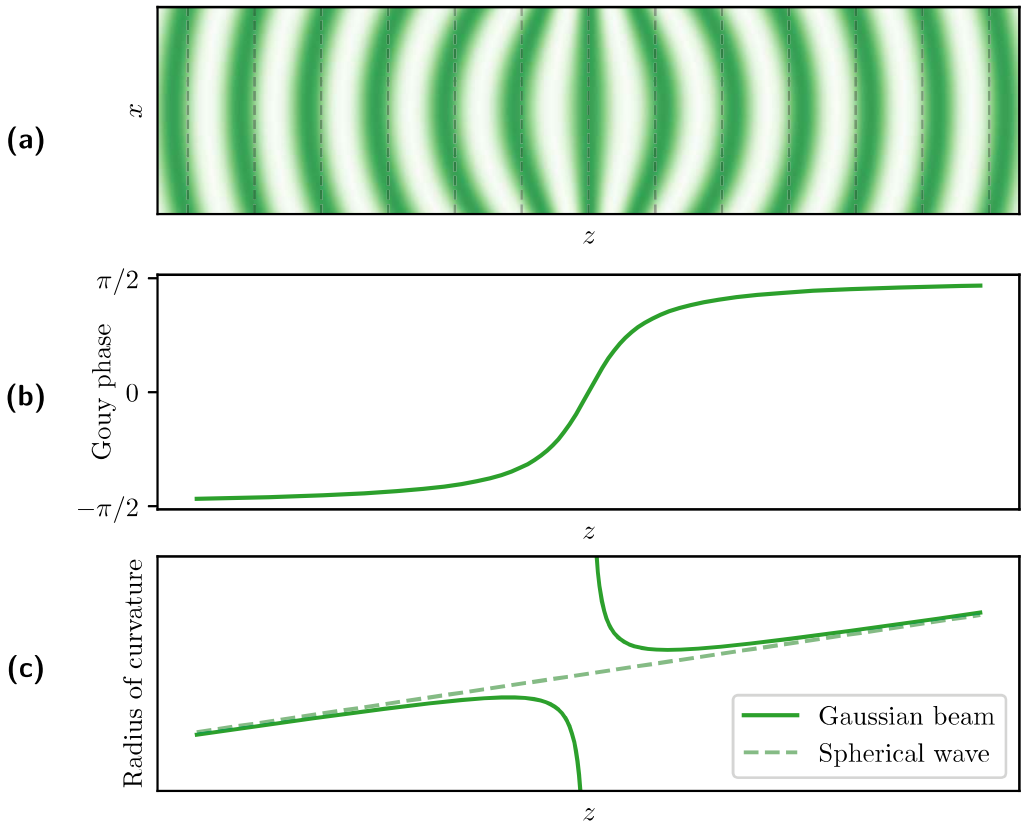

Figure 2.5: (a) Gaussian wavefronts along z. The dashed lines represent the wavefronts of a plane wave. It is easy to see that along the beam axis z (along which the wavefronts are symmetrical), there is a phase difference between the Gaussian beam and the plane wave. It is determined by the second term in equation (2.21) and is visualised below. **(b)** The Gouy phase describes the phase retardation on the beam axis of a Gaussian beam with respect to a plane wave. It vanishes at the beam waist and increases to a maximum of $\pm\pi/2$ on each side. **(c)** This plot shows the radius of curvature $R(z)$ of the Gaussian wavefronts for different positions along the beam, according to equation (2.10). To the left of the beam waist, the radius is negative while on the right side it is positive. At the beam waist it becomes infinite which corresponds to a wavefront with no curvature. The dashed line shows the radius of curvature for the wavefronts of a spherical wave. We can see that further away from the beam waist, the wavefronts of a Gaussian beam resemble those of a spherical wave.

2.1.2 Optical Components and Transfer Matrices

Optical components that a beam propagates through change its geometry. There are several ways to describe the transformation to the beam mathematically, one of which will be briefly discussed here.

Transfer matrices are 2×2 matrices, typically used in geometrical (ray) optics for paraxial waves in an assumed planar geometry. It simplifies the mathematical propagation of rays through a large series of optical elements by representing the properties of the ray in a vector and assigning every optical component a matrix that transforms the vector. A chain of optical components becomes the multiplication of several matrices. The vector describing the ray consists of a position x and an angle θ with respect to the optical axis.

$$\begin{pmatrix} x_2 \\ \theta_2 \end{pmatrix} = \underbrace{\begin{pmatrix} A & B \\ C & D \end{pmatrix}}_{\substack{\text{Transfer matrix,} \\ \text{or product of} \\ \text{transfer matrices}}} \begin{pmatrix} x_1 \\ \theta_1 \end{pmatrix} \tag{2.23}$$

Different optical components, as well as a propagation through free space, are represented by different types of transfer matrices, the most common of which are shown in table 2.1.

For the propagation of Gaussian beams, the same matrices can be used. Again, the light beam itself is represented by a vector, in the case of Gaussian beams it is $(q, 1)$, with the q-factor that was introduced in equation (2.9). In addition to multiplying this by a matrix, there is also a normalisation factor to keep the second vector entry at 1. Therefore, the transformation can be calculated via

$$\begin{pmatrix} q_2 \\ 1 \end{pmatrix} = \frac{1}{Cq_1 + D} \begin{pmatrix} A & B \\ C & D \end{pmatrix} \begin{pmatrix} q_1 \\ 1 \end{pmatrix} \tag{2.24}$$

$$\Rightarrow \; q_2 = \frac{Aq_1 + B}{Cq_1 + D} \,. \tag{2.25}$$

Despite this different calculation of the propagation, it is still possible to multiply several matrices before determining the new q using equation (2.25).

2.1.3 Gaussian Modes

The Gaussian beam seen above is a special solution to the paraxial Helmholtz equation, but it is far from the only one. Several other solutions that exist even share the wavefronts of the Gaussian beam.

We will see later in section 2.2.1 that matching wavefronts to the radii of spherical mirrors is relevant for incoupling light into optical resonators – one can therefore also speak of resonator modes.

Table 2.1: Shown below are the transfer matrices for different optical components as well as for free space propagation. The advantage of using transfer matrices lies in the possibility that for large optical setups with several different components, the propagation of a ray or beam does not have to be carried out step by step. Rather, the transfer matrices of the individual components can be multiplied first and then the propagation can be made with just the one resulting transfer matrix.

Optical element	Transfer matrix
Free space propagation over distance d	$\begin{pmatrix} 1 & d \\ 0 & 1 \end{pmatrix}$
Reflection from a flat mirror	$\begin{pmatrix} 1 & 0 \\ 0 & 1 \end{pmatrix}$
Reflection from a spherical mirror with effective radius R_{eff}	$\begin{pmatrix} 1 & 0 \\ -\frac{2}{R_{\text{eff}}} & 1 \end{pmatrix}$
Thin lens with focal length f	$\begin{pmatrix} 1 & 0 \\ -\frac{1}{f} & 1 \end{pmatrix}$

First, we consider the Gaussian beam envelope $A(\boldsymbol{r})$ from equation (2.8). This envelope can be modulated with some real functions $\mathcal{X}(\,\cdot\,)$, $\mathcal{Y}(\,\cdot\,)$, and $\mathcal{Z}(\,\cdot\,)$ in x, y, and z. If the modulation is of the form

$$A'(\boldsymbol{r}) = \mathcal{X}\left(\sqrt{2}\frac{x}{w(z)}\right)\mathcal{Y}\left(\sqrt{2}\frac{y}{w(z)}\right)e^{i\mathcal{Z}(z)}A(\boldsymbol{r})\,, \tag{2.26}$$

then the corresponding beam exhibits a non-Gaussian intensity distribution but shares the wavefronts with the Gaussian beams. The paraxial Helmholtz equation puts additional constraints on the modulating functions, which leads – after some transformations and substitutions – to the Hermite equation for $\mathcal{X}$ and $\mathcal{Y}$, solved by the Hermite polynomials $H_n(\,\cdot\,)$. A solution can be denoted by a tuple (l, m) where

$$\mathcal{X}(\,\cdot\,) = H_l(\,\cdot\,) \tag{2.27}$$

$$\mathcal{Y}(\,\cdot\,) = H_m(\,\cdot\,)\,, \tag{2.28}$$

with $\mathcal{Z}$ following as

$$\mathcal{Z}(z) = (l+m)\arctan\left(\frac{z}{z_0}\right)\,. \tag{2.29}$$

The complex amplitude of the so called Hermite-Gaussian (HG) beam of order (l, m) is thus

$$\begin{aligned} U_{l,m}(\boldsymbol{r}) = A_{l,m}\,\frac{w_0}{w(z)}\,H_l\left(\sqrt{2}\frac{x}{w(z)}\right)\,H_m\left(\sqrt{2}\frac{x}{w(z)}\right)\exp\left[-\frac{x^2+y^2}{w^2(z)}\right] \\ \cdot\exp\left[-ik\frac{x^2+y^2}{2R(z)} + i(l+m+1)\arctan\left(\frac{z}{z_0}\right) - ikz\right]\,. \end{aligned} \tag{2.30}$$

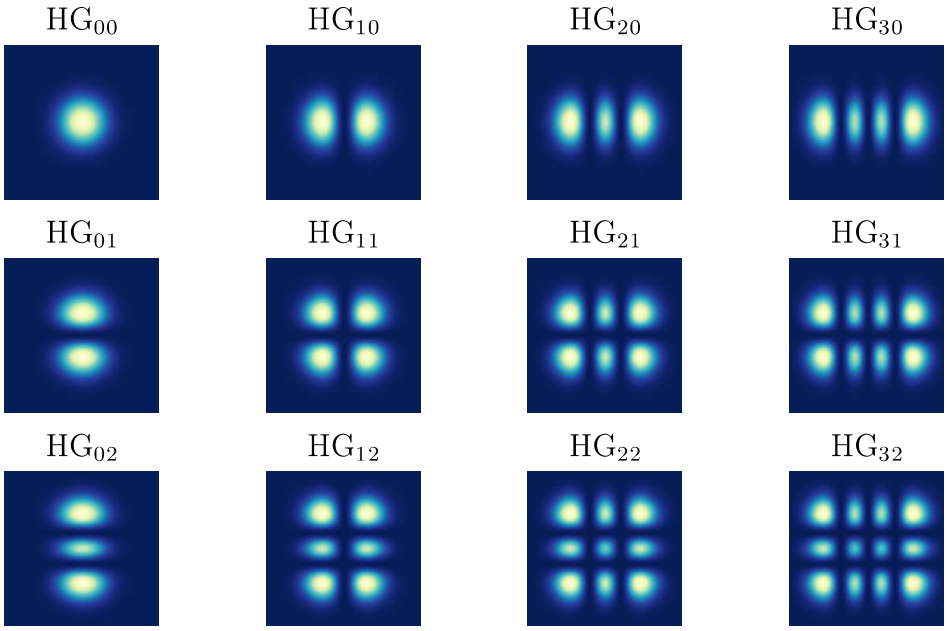

Figure 2.6: The first few orders of Hermite-Gaussian modes are depicted, where the order (0,0) is the fundamental Gaussian beam. They are derived by modulating the amplitude of the Gaussian beam and solving the paraxial Helmholtz equation which they are a complete set of solutions for.

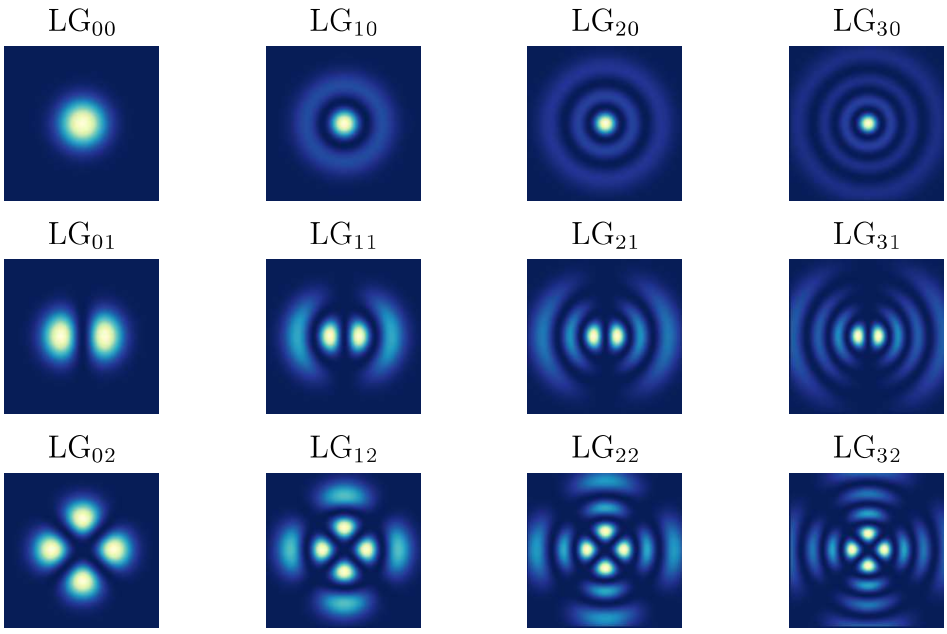

Figure 2.7: If cylindrical coordinates are used in the derivation of further modes, one arrives at the Laguerre-Gaussian modes, the first few orders of which are shown here. Again, the order (0,0) produces the fundamental Gaussian beam.

We can see that the Gouy phase shift is stronger than that of the Gaussian beam by a factor of $1 + l + m$. The intensity distributions of the first few Hermite-Gaussian modes are depicted in figure 2.6.

The Hermite-Gaussian modes are a complete set of solutions of the paraxial Helmholtz equation, meaning every other solution can be expressed as a linear combination of these modes. They are not the only complete set – with a similar derivation, using cylindrical coordinates instead of x and y, one arrives at a different set of solutions, the so called Laguerre-Gaussian beams. They are also numbered by a pair of indices (l, m), denoting the radial and azimuthal index, respectively, and the factor determining the stronger Gouy phase shift is $1 + 2l + |m|$. The intensity distributions of the lowest order LG beams are displayed in figure 2.7.

2.2 Optical Resonators

Optical resonators or resonant optical cavities are systems of optical components where incoupled light continuously repeats a closed path. They confine a light field in the directions perpendicular to their propagation. Different configurations of optical resonators exist – they can be waveguided or through free space; or they can have a ring-like or linear arrangement. The repeated reflections and their superposition within the resonator leads to the formation of discrete modes with different resonant frequencies. One differentiates between longitudinal modes and transversal modes, both of which are discussed below.

Optical resonators have numerous applications, the most important is that they are the basic building block for lasers, where a gain medium is placed inside the cavity to generate coherent light. Other applications include the selection of a certain optical frequency or intensity profile by selecting the relevant mode [38, 39], using the high intracavity intensities for non-linear optical effects [40, 41], cavity ring-down spectroscopy to measure low-level losses [42], or using them as short-term frequency standards [23, 43].

2.2.1 Fabry-Pérot Resonator

The derivations presented in this section are based on [37] and [44].

A stable optical cavity consists of two (or sometimes more) mirrors in which the light will eventually replicate itself. Two parallel mirrors arranged at a distance d make up the most simple form of linear resonator, often called a Fabry-Pérot resonator or cavity. An incoming beam can be effectively coupled into the fundamental cavity mode if it fulfills the following two incoupling conditions:

1. Matching the spatial dimensions of the incoming beam to that of the fundamental cavity mode. This is related to the different transversal electromagnetic (TEM) modes of the resonator.

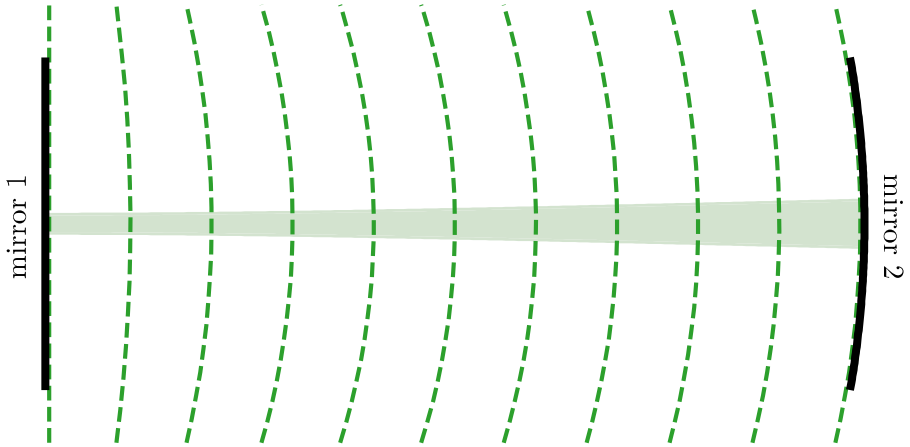

Figure 2.8: This figure demonstrates conditions of spatial incoupling into a planar-spherical cavity of length d. To match the wavefronts to the surface of both mirrors, the waist of the Gaussian beam has to coincide with the planar mirror. The Rayleigh length z_0 (and hence the waist radius w_0) follows from the radius of curvature R_2 of the spherical mirror, as equation (2.34) reduces to $z_0^2 = d(R_2 - d)$ for $R_1 = \infty$.

2. Ensuring that the phase of the light is self-reproducing after one round-trip inside the cavity. This leads to standing waves inside linear resonators and to their longitudinal modes.

Strictly speaking, the definition of a Fabry-Pérot cavity specifies two planar mirrors, the name is, however, also often used for a linear arrangements of two curved mirrors – such is the case here. For a Fabry-Pérot cavity made up of two mirrors with radii of curvature R_1 and R_2, the first condition concerning the spatial replication is fulfilled if the light beam's wavefront coincides with the mirror surfaces. In this case, the reflected beam exactly overlaps with the incident beam and no amount of cycles of the light back and forth results in the light beam leaving the resonator. This spatial incoupling is visualised in figure 2.8.

Since the beam's wavefront radius $R(z)$ has to match the mirror curvatures R_1 and R_2 at a distance d from each other, we can, with the help of equation (2.10), write

$$z_2 - z_1 = d\,, \tag{2.31}$$

$$R(z_1) = z_1 \left(1 + \left(\frac{z_0}{z_1}\right)^2\right) = -R_1\,, \tag{2.32}$$

$$R(z_2) = z_2 \left(1 + \left(\frac{z_0}{z_2}\right)^2\right) = R_2\,. \tag{2.33}$$

Note the convention in equation (2.32) for negative radius of curvature to the left of the beam waist, while both R_1 and R_2 are assumed to be positive for concave mirrors. The mirror positions with respect to the beam waist are given by z_1 and z_2, and z_0 denotes the beam's Rayleigh length.

To determine these three unknown parameters, the above equations (2.31) to (2.33) can be rewritten as

$$z_0^2 = \frac{d(R_1 - d)(R_2 - d)(R_1 + R_2 - d)}{(R_1 + R_2 - 2d)^2}\,, \tag{2.34}$$

$$z_1 = \frac{-d(R_2 - d)}{R_1 + R_2 - 2d}\,, \tag{2.35}$$

$$z_2 = \frac{d(R_1 - d)}{R_1 + R_2 - 2d}\,. \tag{2.36}$$

This fully defines the beam in the cavity setup – if the solution above exists. If that is not the case, if for a mirror configuration of R_1, R_2, and d it is not possible for the beam to replicate itself and to match the Gaussian beam's wavefronts to the mirrors, then the cavity is called unstable.

The configurations where no stable cavity setup is possible can be most easily expressed using the so called g-parameters

$$g_i = \left(1 + \frac{d}{R_i}\right) \quad \text{, where } i = 1, 2\,, \tag{2.37}$$

the stability condition can be written as

$$0 \leq g_1\, g_2 \leq 1\,. \tag{2.38}$$

At this point, it should be mentioned that it is also possible to determine the beam parameters with the matrix formalism that was briefly introduced in section 2.1.2. The q parameter of the matching Gaussian beam will be mapped onto itself by equation (2.25) with the transfer matrix made up of the cavity components.

With the spatial condition taken care of, we neglect it henceforth and only consider the light field of a plane wave as we take a closer look at the second criterion. The resonance condition for a monochromatic standing wave of wavelength λ and frequency $f = c/\lambda$ in a linear resonator is

$$n\frac{\lambda}{2} = d \quad \Leftrightarrow \quad f = n\frac{c}{2d}\,, \tag{2.39}$$

where c is the speed of light and n is a natural number. Is this condition fulfilled, the wave forms a standing wave inside the resonator, for each n a different number of oscillations

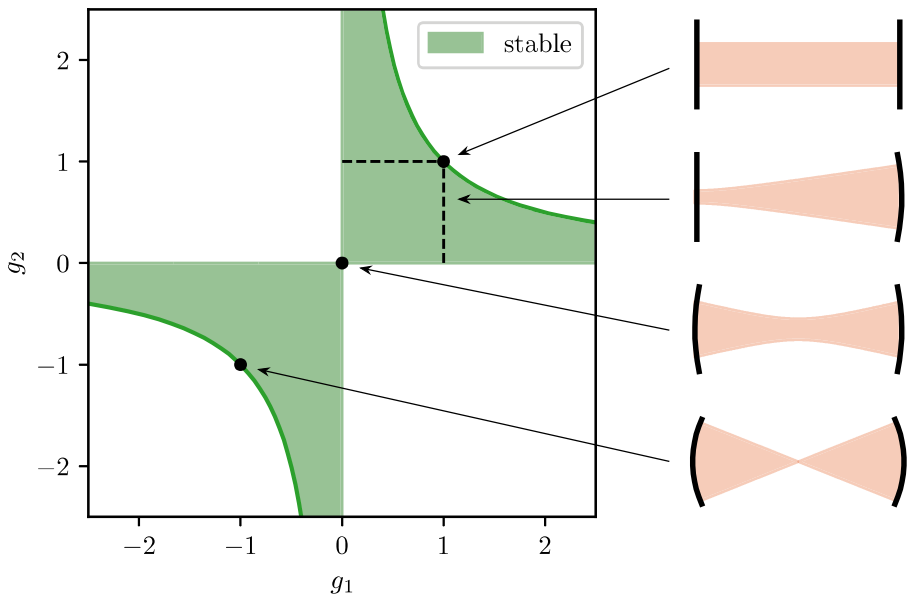

Figure 2.9: Stability diagram for linear cavities of length d with two spherical mirrors, where the region of stability parameters g_1 and g_2 (see equation (2.37)) allowing a self-replicating beam, is marked in green. Some cavity geometries are pointed out, from top to bottom there are: a planar cavity where $R_1 = R_2 = \infty$; the region of spherical-planar cavities where either $R_1 = \infty$ or $R_2 = \infty$; a confocal cavity where $R_1 = R_2 = d$; a concentric cavity where $R_1 = R_2 = d/2$.

between the mirrors. These are called the longitudinal modes of the resonator. It is easy to see that the frequencies of neighbouring resonator modes differ by

$$\nu_{\mathrm{FSR}} = \frac{c}{2d}\,. \tag{2.40}$$

This is called the free spectral range ν_{FSR} of the cavity.

To understand the light field inside and after the resonator, one first considers the two mirrors with finite reflectivities for the electric field r_1 and r_2. To simplify the formulas, they are assumed to be the same here, $r_1 = r_2 = r$. Each time the light encounters a mirror, a part of it gets reflected and another part is transmitted, according to the mirror reflectivity; this is visualised in figure 2.10. The incoming light with amplitude E_0 enters the cavity through one of the mirrors, its amplitude being $t \cdot E_0$ on its first passage, with the transmission coefficient $t = \sqrt{1 - r^2}$ (assuming no losses) of the mirrors. For each cycle inside the resonator, the amplitude decreases. Once the light has passed through the resonator in both directions, the resulting field E_1 can be described by

$$E_1 = r^2\, e^{i\varphi} t E_0\,, \tag{2.41}$$

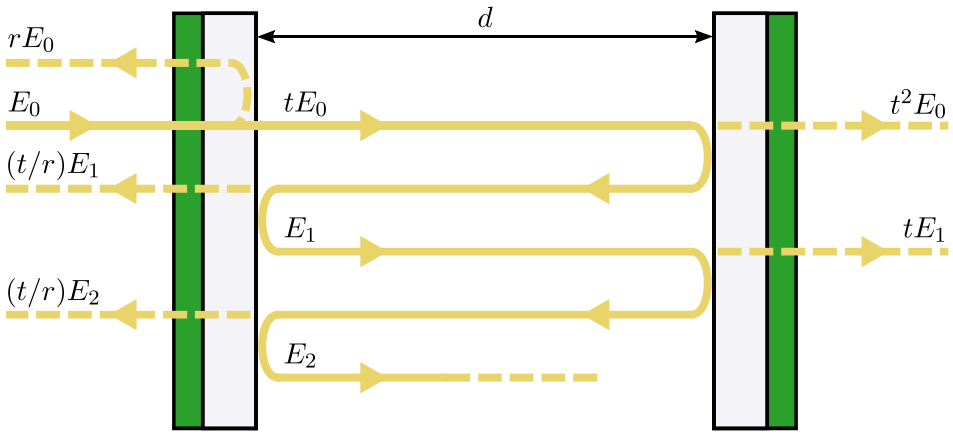

Figure 2.10: Scheme of a Fabry-Pérot resonator of length d. Here, all the light beams that would overlap in reality are shown separately. A part of the incoming beam E_0 is reflected at the first mirror, while the other part enters the resonator. Inside the cavity, the light is reflected back and forth with some of the intensity leaking out of the resonator at every reflection, such that after m such cycles it is described by E_m. The outgoing light adds to the total transmission or reflection, depending on which mirror the light leaks out off.

where

$$\varphi = 4\pi f d/c = 2\pi f/\nu_{\mathrm{FSR}} \tag{2.42}$$

is the phase shift relative to the incidental wave, accumulated during one round trip. For each successive cycle, an additional factor of $r^2\, e^{i\varphi}$ needs to be considered such that after m round trips the electric field has become

$$E_m = r^{2m}\, e^{im\varphi} t E_0\,. \tag{2.43}$$

The total electric field E in the resonator results from the superposition of the electric fields after m revolutions in the resonator:

$$E = \sum_{m=0}^{\infty} \left(r^2\, e^{i\varphi}\right)^m t E_0 = \frac{tE_0}{1 - r^2 e^{i\varphi}}\,. \tag{2.44}$$

This results in an intensity I inside the optical resonator of[2]

$$I = |E|^2 = \frac{t^2|E_0|^2}{|1 - r^2 e^{i\varphi}|^2} = \frac{(1-r^2)|E_0|^2}{1 + r^4 - 2r^2\cos\varphi}\,. \tag{2.45}$$

[2]To get the actual physical intensity from the electric light field, a factor of $cn\varepsilon_0/2$ is missing. Since the absolute value is irrelevant here, this factor is neglected.

Defining the maximum intensity $I_{\max}$ and the cavity's finesse $\mathcal{F}$[3] as

$$I_{\max} = \frac{|E_0|^2}{(1-r^2)} \quad \text{and} \tag{2.46}$$

$$\mathcal{F} = \frac{\pi r}{1-r^2}\,, \tag{2.47}$$

and using the definition of the free spectral range from equation (2.40), equation (2.45) can be rewritten as

$$I = \frac{I_{\max}}{1 + (2\mathcal{F}/\pi)^2 \sin(\pi f/\nu_{\mathrm{FSR}})}\,. \tag{2.48}$$

This so called spectral response of the resonator can be seen in figure 2.11 for optical cavities with different finesse. It can be noted that the intensity peaks that repeat every free spectral range are thinner the higher the finesse is. A higher finesse indicates higher mirror reflectivities which leads to more back-and-forth cycles of the light inside the resonator that contribute to the interfering fields. The more additional fields can counteract the incoming field, the closer the resonance condition has to be met and the narrower the peaks are. For sharp resonances ($\mathcal{F} \gg 1$), the peaks can be approximated by a Lorentzian function that has the full width half maximum (FWHM)

$$\Delta\nu = \frac{\nu_{\mathrm{FSR}}}{\mathcal{F}}\,, \tag{2.49}$$

called the cavity linewidth.

The transmitted light is similar to the added up light inside the resonator, except for an additional factor of t for each cycle, as a small fraction of the built-up light leaves the cavity. For the total transmitted light E_{trans} and its intensity I_{trans} follows, analogous to the derivations above,

$$E_{\mathrm{trans}} = \sum_{m=0}^{\infty} \left(r^2\, e^{i\varphi}\right)^m t^2 E_0 = \frac{t^2 E_0}{1 - r^2 e^{i\varphi}}\,, \tag{2.50}$$

$$I_{\mathrm{trans}} = \frac{|E_0|^2}{1 + (2\mathcal{F}/\pi)^2 \sin(\pi f/\nu_{\mathrm{FSR}})}\,. \tag{2.51}$$

Besides the fields in and after the resonator, the reflected field E_{refl} counterpropagating to the incoming light is also of interest. A part of the incoming light is reflected before even entering the cavity and interferes with the light that leaks from inside the cavity every cycle. Therefore, the sum for the total reflected light field follows as

$$\begin{aligned} E_{\mathrm{refl}} &= rE_0 - \sum_{m=1}^{\infty} \left(r^2\, e^{i\varphi}\right)^m \frac{t^2}{r} E_0 \\ &= rE_0 - \frac{t^2 r E_0 e^{i\varphi}}{1 - r^2 e^{i\varphi}} \end{aligned} \tag{2.52}$$

[3] This definition of the finesse is valid for low-loss and high reflectivity cavities ($1 - r \ll 1$).

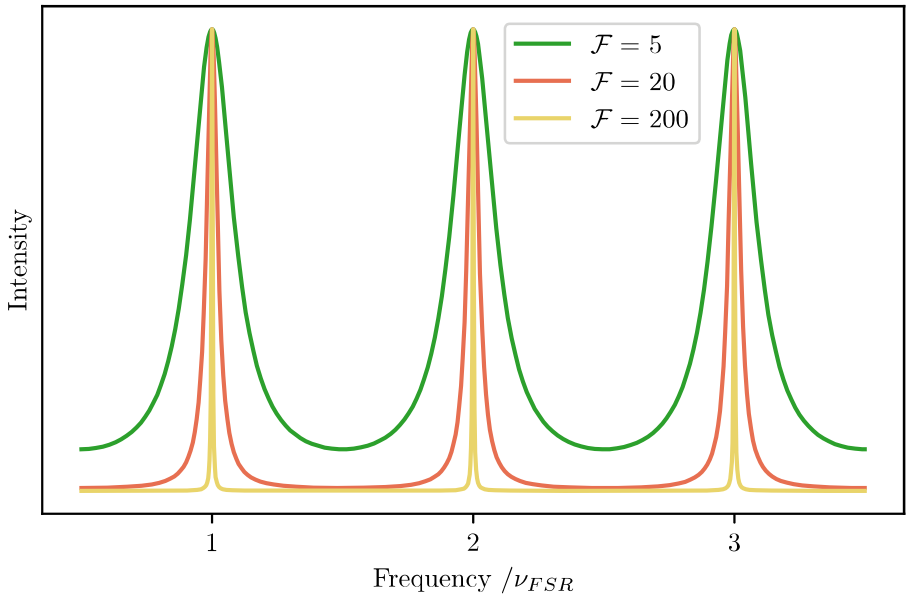

Figure 2.11: Maximum intensity build up inside Fabry-Pérot cavities of the same length and different finesse, depending on the incoming light frequency. This is sometimes also called the spectral response of a cavity. As expected, it exhibits a periodic behaviour, with peaking intensities repeating every free spectral range ν_{FSR}. We can see clearly that the width of the peaks depend on the finesse, with much thinner peaks for higher values of finesse. Both the behaviour of the transmitted cavity light and the maximum intensities inside the cavity can be described by this graph, as they are proportional to each other (see equations (2.48) and (2.51)). However, the maximum value of the transmitted light for loss-less mirrors is equal to that of the incoming light, whereas the intracavity intensities can be much higher, increasing further with higher finesse.

The difference in sign between the two terms follows from the 180° phase jump the light wave gets when reflected from a material with a higher refraction index, like the light inside the cavity propagating through air or vacuum, reflected at a mirror made of glass. Hence, the incoming light reflecting from the inside of the mirror before entering the cavity does not get this phase shift.

Dividing the reflected field by the total incoming light E_0, we get the so called reflection coefficient $F(\omega)$, typically given as a function of the angular light frequency ω. After some transformations it reads

$$F(\omega) = \frac{E_{\text{refl}}}{E_0} = r\frac{1 - e^{i\varphi}}{1 - r^2 e^{i\varphi}}\,. \tag{2.53}$$

2.2.2 Pound-Drever-Hall Locking

Lasers are nearly monochromatic, but they have a spectrum of noise that through frequency fluctuations contributes to a finite linewidth. Hence, there are different timescales that broaden the laser's spectrum. While a faster noise – usually caused by statistical processes in the laser medium – broadens the laser linewidth, slower noise – e.g. due to external perturbations or temperature changes – can cause 'jitters' or drifts of the spectral line.

A reduction of noise can be achieved by constantly measuring the difference from the desired frequency (this is usually called the error) and to electronically feed this back to the laser to steer it toward the target value. Optimal results are achieved if the bandwidth of the electronic servo is larger than the dominant noise in the laser's noise spectrum.

A resonator, such as described above, can be used for stabilisation of a laser wavelength, given it is more stable than the laser source. This involves keeping the length of the cavity very stable and, with a feedback loop, keeping the laser's wavelength in the resonance condition. Utilising the transmission signal, which peaks at the resonance, is inconvenient for a number of reasons. To generate a feedback signal, there are at least two measurements required per cycle. Additionally, the transmission depends on the total incoming power, so the feedback would be susceptible to power fluctuations.

A widely used method for stabilising a laser to an optical resonator is the so called Pound-Drever-Hall (PDH) technique, named after Robert Pound, Ronald Drever, and John Lewis Hall. The first instance of this method being used was in 1983 by Drever and Hall [43]. Some decades earlier, a similar technique was invented and used by Pound in the microwave regime [45].

The reflection intensity of a monochromatic beam or wave has a minimum at the resonance frequency, the phase difference to the incoming field has a zero crossing, as was seen in equation (2.53). For a locking feedback, one ideally wants a zero crossing in the measured signal, but the phase is not normally accessible. Instead, the incoming light is modulated such that the interference with reflected sidebands extracts the phase information from the reflection signal.

A typical PDH scheme can be seen in figure 2.12. The following mathematical approach is based on ref. [46].

The incoming light field $e^{i2\pi ft} = e^{i\omega t}$ is modulated in its phase with an RF oscillation; typically this is achieved with an electro-optical modulator. Neglecting the spatial distribution of the beam, the incident light field reads

$$E_{\mathrm{inc}} = E_0\, e^{i\omega t} \rightarrow E_0\, e^{i\omega t + \beta \sin(\omega_{\mathrm{m}} t)}\,. \tag{2.54}$$

Here, β is the modulation depth which determines the strength of the modulation whereas ω_{m} denotes the modulation frequency. With the help of the Bessel functions, this formula

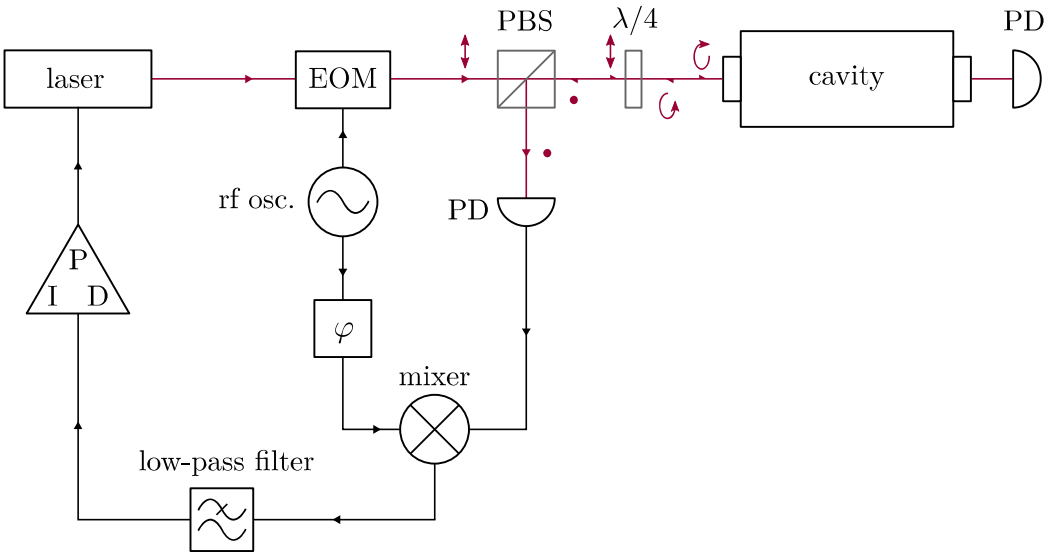

Figure 2.12: Shown here is a basic Pound-Drever-Hall (PDH) feedback loop for locking a laser to an optical cavity. Laser light is sent through an electro-optical modulator (EOM) for phase modulation with a sine signal to generate sidebands and is then coupled into the cavity. A combination of a polarising beam splitter (PBS) and a quarter-waveplate ($\lambda/4$) ensures that the light in the two propagation directions – incoming and reflected from the cavity – can be distinguished. The incoming light goes straight through the PBS while the reflected light, consisting of reflected carrier and sidebands, is sent to a photodetector (PD). In the picture, the arrows next to the laser beam illustrated in red indicate the polarisation of the light that makes this possible. The sinusoidal signal driving the phase modulator is mixed with this reflected signal (its phase can be adjusted with a phase shifter denoted with φ). This demodulates the signal and shifts the interference between the carrier and the sidebands to a dc signal which is then isolated with a low-pass filter. A PID controller translates the resulting error signal into a feedback signal for the laser.

can be simplified. The Bessel functions $J_n(\beta)$, represented with the integral definition, read

$$J_n(\beta) = \frac{1}{2\pi}\int_{-\pi}^{\pi} e^{i\beta\sin(x)}e^{-inx}dx\,. \tag{2.55}$$

This representation shows that the Bessel functions are the Fourier series coefficients of the function $e^{i\beta\sin(x)}$, hence we can write

$$\begin{aligned} E_{\text{inc}} &= E_0\, e^{i\omega t}e^{\beta\sin(\omega_{\text{m}}t)} \\ &= E_0\, e^{i\omega t}\sum_{n=-\infty}^{\infty} J_n(\beta)e^{in\omega_{\text{m}}t} \\ &\approx E_0\left[J_0(\beta)\, e^{i\omega t} + J_1(\beta)\, e^{i(\omega+\omega_{\text{m}})t} + J_{-1}(\beta)\, e^{i(\omega-\omega_{\text{m}})t}\right]. \end{aligned} \tag{2.56}$$

In the last step, indices n other than 0 and ± 1 were neglected, which is a good approximation for $\beta < 1$. This also demonstrates that in first order, the light can be treated as three beams with different frequencies, a carrier of frequency ω and two sidebands with $\omega \pm \omega_\mathrm{m}$.

For the reflection of this modulated light, the sidebands are considered separately, as they each have different reflection coefficients depending on their frequency according to equation (2.53).

$$\begin{aligned} E_\mathrm{refl} = E_0 \Big[& F(\omega) J_0(\beta)\, e^{i\omega t} + F(\omega+\omega_\mathrm{m}) J_1(\beta)\, e^{i(\omega+\omega_\mathrm{m})t} \\ & + F(\omega-\omega_\mathrm{m}) J_{-1}(\beta)\, e^{i(\omega-\omega_\mathrm{m})t} \Big] . \end{aligned} \tag{2.57}$$

After this light is reflected from the optical cavity, the intensity is measured with a photodetector, for instance a photodiode. To get the intensity, the light field is squared. Several algebraic transformations later, it reads

$$\begin{aligned} I_\mathrm{refl} &= |E_\mathrm{refl}|^2 \\ &= I_\mathrm{c} |F(\omega)|^2 + I_\mathrm{s} |F(\omega+\omega_\mathrm{m})|^2 + I_\mathrm{s} |F(\omega-\omega_\mathrm{m})|^2 \\ &\quad + 2\sqrt{I_\mathrm{c} I_\mathrm{s}}\, \mathrm{Re}\left[F(\omega) F^*(\omega+\omega_\mathrm{m}) - F^*(\omega) F(\omega-\omega_\mathrm{m}) \right] \cos(\omega_\mathrm{m} t) \\ &\quad + 2\sqrt{I_\mathrm{c} I_\mathrm{s}}\, \mathrm{Im}\left[F(\omega) F^*(\omega+\omega_\mathrm{m}) - F^*(\omega) F(\omega-\omega_\mathrm{m}) \right] \sin(\omega_\mathrm{m} t) \\ &\quad + (2\,\omega_\mathrm{m} \text{ terms}) . \end{aligned} \tag{2.58}$$

To improve legibility, the intensities of the carrier and the sidebands were defined as

$$I_\mathrm{c} = J_0^2(\beta) |E_0|^2 \quad \text{and} \tag{2.59}$$

$$I_\mathrm{s} = J_1^2(\beta) |E_0|^2 = J_{-1}^2(\beta) |E_0|^2 , \tag{2.60}$$

respectively. The sum of three waves of different frequency result in contributions to the intensity that oscillate in time at multiples of the modulation frequency in addition to a constant part. The terms in equation (2.58) oscillating with the modulation frequency ω_m come from the interference of the carrier and each sideband. There is also a term oscillating with $2\,\omega_\mathrm{m}$ from the sidebands interfering with each other, but this is not important for the PDH method and therefore neglected here.

A photodetector of high enough bandwidth records all parts of equation (2.58), and the relevant parts with $\cos(\omega_\mathrm{m} t)$ and $\sin(\omega_\mathrm{m} t)$ are isolated with a mixer and a subsequent low-pass filter. A mixer generates a product of the inputs, one of them is the measured reflected intensity, while the other is the oscillation that has also been used for the phase-modulation. We remember that the product of two sine waves (or two cosine waves) is the sum of a cosine of the difference of the frequencies and a cosine of the summed up frequencies, hence, after mixing the reflection signal with an oscillation of ω_m, the resulting signal has a constant part which can be isolated with a low-pass filter. A phase shifter for the mixing oscillation is typically installed in the setup to ensure

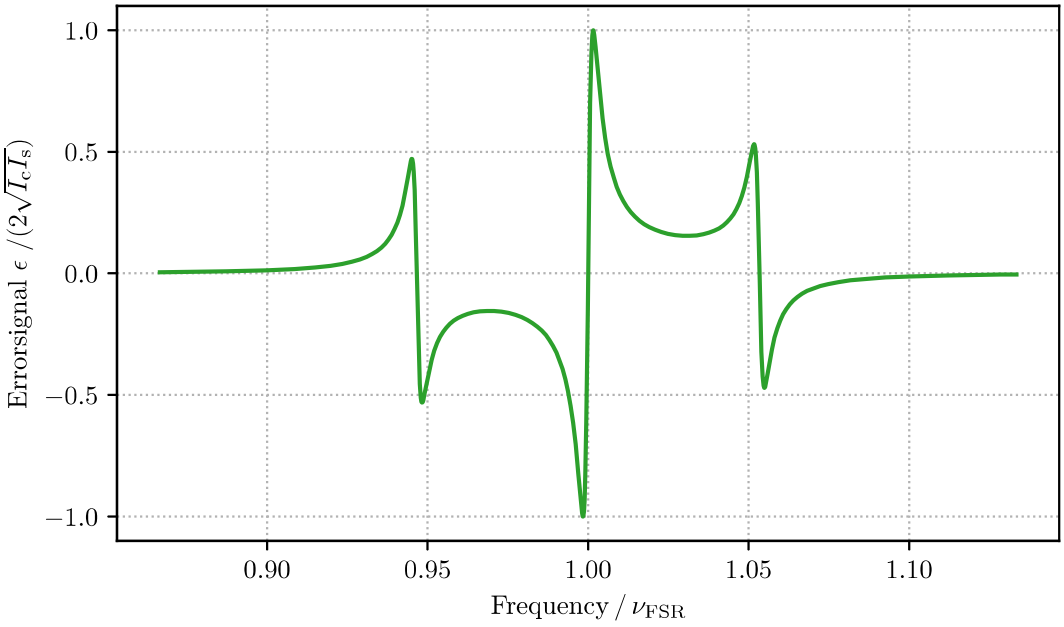

Figure 2.13: A PDH error signal according to equation (2.61), such that the modulation frequency ω_m is large compared to the cavity linewidth. In this graph, the modulation frequency corresponds to about 30 linewidths and 5 % of the FSR.

matching phases, otherwise a necessary phase shift needs to be introduced via delay lines.

For a modulation frequency high enough to ensure that the resonances of the sidebands and the carrier are distant enough from each other, the relevant term in equation (2.58) becomes purely imaginary. The cosine term becomes negligible and with suitable phase matching of the mixing signal and subsequent low-pass filtering the resulting error signal ϵ is therefore

$$\epsilon = 2\sqrt{I_\mathrm{c} I_\mathrm{s}}\,\mathrm{Im}\left[F(\omega)F^*(\omega+\omega_\mathrm{m}) - F^*(\omega)F(\omega-\omega_\mathrm{m})\right]\,. \tag{2.61}$$

This can be seen in figure 2.13. The signal has a zero crossing and a linear behaviour at the resonance frequency.

Near the resonance, where the reflection coefficient of the sidebands becomes 1, equation (2.61) can be simplified to

$$\begin{aligned}\epsilon &= 2\sqrt{I_\mathrm{c} I_\mathrm{s}}\;2\,\mathrm{Im}\left[F(\omega)\right] \\ &= 4\sqrt{I_\mathrm{c} I_\mathrm{s}}\;\frac{r(r^2-1)\,\sin\varphi}{1+r^4-2r^2\,\cos\varphi}\,.\end{aligned} \tag{2.62}$$

Linearly expanding this equation around the resonance leads to the following expression:

$$\begin{aligned}\epsilon &\approx 4\sqrt{I_\mathrm{c} I_\mathrm{s}}\,\frac{r}{1-r^2}\varphi \\ &= \frac{4}{\pi}\sqrt{I_\mathrm{c} I_\mathrm{s}}\,\frac{\omega}{\Delta\nu} \\ &= 8\sqrt{I_\mathrm{c} I_\mathrm{s}}\,\frac{f}{\Delta\nu}\,,\end{aligned} \tag{2.63}$$

where the expressions for the round trip phase φ, the finesse $\mathcal{F}$ and the cavity linewidth $\Delta\nu$ – see equations (2.42), (2.47) and (2.49), respectively – were used.

2.2.3 Limits and Noise

Following from equation (2.63), a small deviation δf of the laser frequency from the resonance leads to a signal of

$$\delta\epsilon = 8\sqrt{I_\mathrm{c} I_\mathrm{s}}\,\frac{2d\mathcal{F}}{\lambda}\,\frac{\delta f}{f}\,. \tag{2.64}$$

Additionally, it can be shown that a change in the length of the resonator δd has a comparable effect on the error signal, and in total it can be written as

$$\delta\epsilon = 8\sqrt{I_\mathrm{c} I_\mathrm{s}}\,\frac{2d\mathcal{F}}{\lambda}\left(\frac{\delta f}{f} + \frac{\delta d}{d}\right)\,. \tag{2.65}$$

For a given error signal, it is impossible to determine if the source is frequency noise or cavity noise. However, the point of the zero crossing is insensitive to changes in the laser power, response of the photodetector that measures the reflection signal, the modulation depth β and frequency ω_m, and the phase difference of the signals going into the mixer.

On the order of the modulation frequency ω_m, there is a sensitivity to fluctuations in the sideband power, decreasing for higher frequency. By increasing the modulation frequency, this noise source can usually be reduced so it is not relevant anymore.

One noise source that cannot be reduced this way, due to its flat frequency spectrum, is shot noise. As it results from the quantisation of the light itself, it introduces a fundamental limit to how noiseless an error signal can be. An estimation for the spectral density of the shot noise of the error signal S_ϵ is given by

$$S_\epsilon = \sqrt{2\frac{hc}{\lambda}\,2I_\mathrm{s}}\,, \tag{2.66}$$

where h is the Planck constant. In equation (2.63) we saw the linear relation of the error signal to the frequency near the resonance, hence, this noise translates to noise on the frequency as

$$S_f = \frac{\sqrt{hc^3}}{8}\,\frac{1}{\mathcal{F}d\sqrt{\lambda I_\mathrm{c}}}\,. \tag{2.67}$$

The frequency cannot be resolved any better, therefore, feedback to the laser via the PDH method can never be more stable than this. It should be noted, that the shot noise for the frequency does not depend on the power of the sidebands, and only on that of the carrier.

Since fluctuations in the laser frequency and in the cavity length cannot be distinguished, another fundamental limitation to the frequency stabilisation has to be considered. The Brownian motion of the cavity components sets the limit of the stability that can be achieved in terms of cavity length. More details on this noise limit can be found in references [23, 47].

Here, we will briefly mention some external factors that introduce noise to the length of the cavity and therefore limit the achievable uncertainty of the laser frequency for a certain setup. The first chapter of [48] gives a good outline of the different effects.

Temperature instabilities can cause a change in the cavity length due to thermal expansion effects. These can be transferred to the cavity spacer through thermal radiation and conduction via air or mounting material. The conduction is small for standard interface materials (including viton) and therefore the conduction through the connections to the mounting can be neglected. For a cavity in vacuum the main heat transfer is via thermal radiation. Thermal shielding stages around the resonator are desirable; they are thermalised from the environment through conduction so ideally they have a large volume and a low thermal conductivity, the latter is also applicable for its supporting structures. A better thermal isolation leads to the resonator length to be sless sensitive to short term temperature fluctuations, which is expressed by the so called thermal response time.

External vibrations that are transferred to the cavity can deform it and change its length. This contributes more to the instability the longer the cavity spacer is. The exact effects depend highly on the cavity and mounting geometries and require investigation through simulation. A good isolation from vibrations is necessary for high precision.

The **pressure** changes the refraction index n of the rest gas inside the cavity and therefore the optical path length. According to [49], a total change in pressure ΔP is proportional to a fractional change in refractive index $\Delta n/n$ with

$$\frac{\Delta n}{n} \approx 2.65 \cdot 10^{-7} \Delta P[\text{mbar}]\,. \tag{2.68}$$

Therefore, fractional pressure fluctuations contribute less to the frequency instability the lower the absolute pressure is.

For cavities with a high finesse, the **intracavity power** increases. A large power leads to localised heating of the cavity mirrors which can change the cavity length through thermal expansion.

So called **residual amplitude modulation** (RAM) can be caused by etalons – optical elements with parallel surfaces that act as their own optical resonator – in the beam

path. This can lead to an additional amplitude modulation at the frequency of the PDH phase modulation and would lead to an instable offset in the error signal which directly leads to frequency instabilities in the locked laser.

3 Stabilisation Setup

The CryPTEx-SC experiment this work is part of, as introduced in section 1.3, aims to realise the ground-level cooling and high precision spectroscopy of HCIs inside a superconducting Paul trap. A narrower linewidth of the spectroscopy laser leads to a decreasing uncertainty of the spectroscopic measurement and can be achieved by directly PDH locking the spectroscopy laser itself to a stable cavity or locking it to a separate stabilised laser.

The work in this thesis marks the first endeavour to realise a stable reference laser in our laboratory to improve future spectroscopy experiments. This chapter gives an overview of the optical cavity and the first mounting (section 3.1), the optical setup that was constructed and the electronics that were used (section 3.2), as well as improvements that have been done or are planned in the near future (section 3.3).

3.1 Optical Cavity and Mounting

The optical resonator used in this work was supplied to our group at the MPIK as a loan from the Physikalisch-Technische Bundesanstalt (PTB)[1]. Figure 3.1 shows a render of this resonance cavity. It is a linear resonator consisting of one planar and one spherical mirror, where the latter has a radius of curvature (ROC) of 1 m. A large ROC leads – according to equations (2.34) to (2.36) – to a relatively large spot size on the mirror surfaces, which in turn results in less thermal noise [50]. The silicon mirrors have a dielectric high-reflection (HR) coating for 1550 nm facing the inside of the resonator and an anti-reflection (AR) coating for the same wavelength facing the outside. They are optically contacted to a cylindrical ultra-low expansion glass (ULE) spacer that has a length of 100 mm. The finesse of the cavity is at least 100 000, which indicates a reflectivity of $> 99.997\,\%$ for each mirror and results in a cavity linewidth of $< 15\,\mathrm{kHz}$.

The coefficient of thermal expansion (CTE) of ULE glass is, as the name suggests, very low. For temperatures from 0 °C to 40 °C its magnitude stays below $30 \cdot 10^{-9}\,\mathrm{K}^{-1}$ with a zero-crossing around a temperature of 20 °C. Since the mirrors are made of silicon, which at room temperature has a CTE of about $2.6 \cdot 10^{-6}\,\mathrm{K}^{-1}$, the CTE and general expansion behaviour of the total cavity differs from that of the spacer alone. Therefore, the zero crossing temperature changes to around 160 K, and the CTE at room temperature on of the order of hundreds of $10^{-9}\,\mathrm{K}^{-1}$. [52]

[1] Thanks goes to Thomas Legero and Piet O. Schmidt.

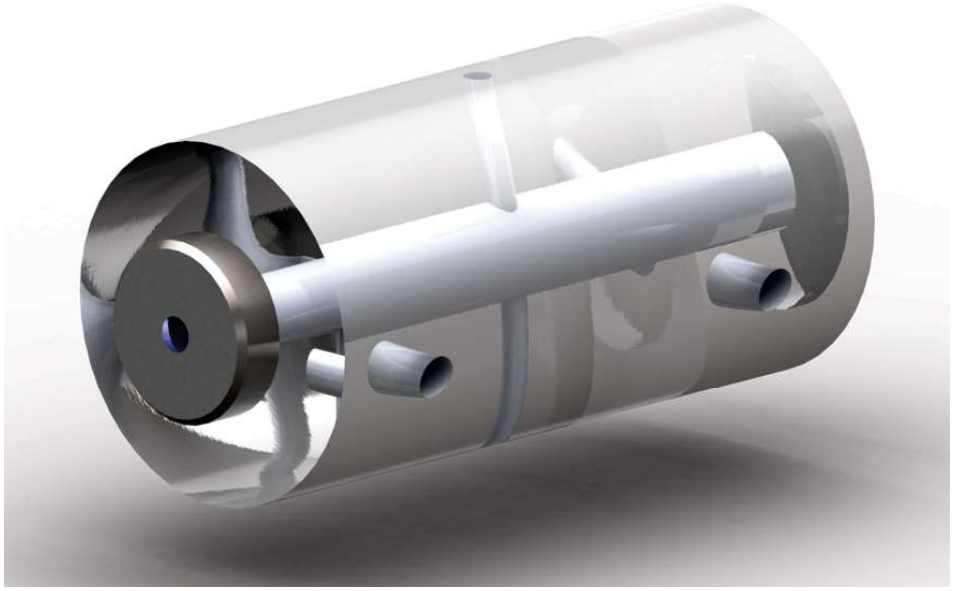

Figure 3.1: Rendered picture of the cavity spacer and mirrors used in this work. The spacer is made of ultra-low expansion (ULE) glass and has a length of 10 cm. The highly reflective silicon mirrors on each side form a planar-spherical optical cavity. They have an anti-reflection coating on the outer side and the spherical mirror has a radius of curvature (ROC) of 1 m. On the side of the cavity spacer, the mounting holes of the cavity can be seen. Their position is optimised to have the least change in length between the mirrors for external vibrations transmitted through the mounting points. [51]

The cylindrical ULE spacer has four mounting holes (see figure 3.1), two on each side along the cavity, slightly below the horizontal symmetry plane. The positions of these holes have been optimised such that the length change of the light path between the mirrors is minimal for transferred external vibrations through the support structure, compare to [53].

Steel pins were constructed to hold the cavity via the mounting holes, where viton rings provide the only point of contact at the centre of the holes. These pins are held by a bronze chamber that surrounds the cavity (see figure 3.2).

The housing in the current setup consists of a hollow bronze cylinder of diameter 100 mm and thickness 22 mm with bronze lids, mounted to the optical table with aluminium feet. The lids have laser windows fitted into the centre. This chamber acts as a shield from external temperature fluctuations. Additionally it has seals all around the screws and openings and is therefore isolated from the outside air and fluctuations due to air flows. While not under vacuum at the time of this thesis, it was built with a potential added vacuum pumping system in mind and should be able to reach a low vacuum.

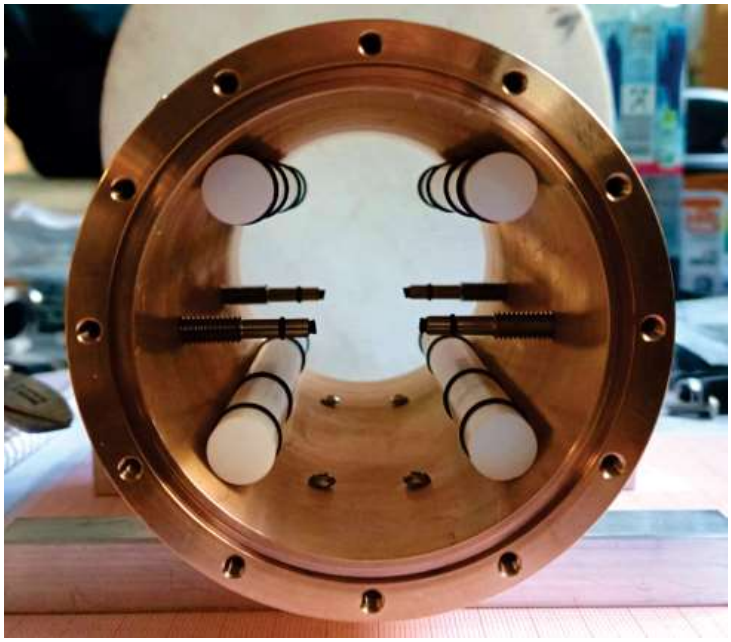

Figure 3.2: Depicted above is the central part of the current bronze cavity housing with the pins used to hold the cavity, visible inside. The white teflon rods do not touch the cavity spacer once it is properly mounted, but help with the process of mounting as well as provide impact protection in case of sudden movements should the mounted cavity be moved. Viton rings on the mounting pins form the point of contact to the spacer and due to their elasticity help reduce the vibrations transferred from the surroundings to the cavity.

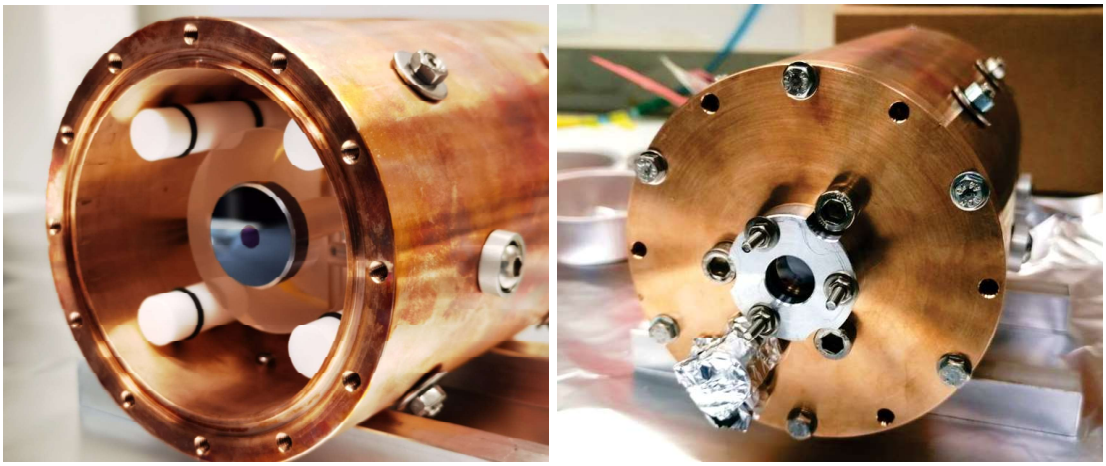

(a) **(b)**

Figure 3.3: (a) Mounted cavity inside the bronze housing. **(b)** When the lids on the front and back are in place, this provides some protection from air flows and short term temperature fluctuations.

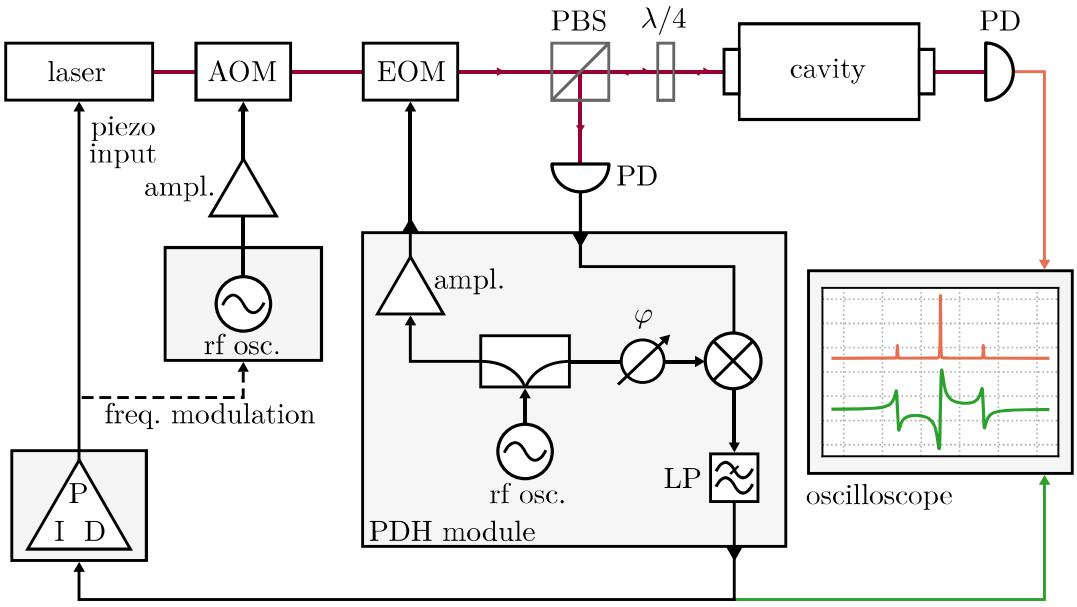

Figure 3.4: Schematic overview of the main electronics used in the setup. For more details on the optical components, see figure 3.5. Most of the necessary electronical components for a PDH setup are included in one PDH module. It contains the rf oscillator and amplifier driving the EOM, and the elements needed to process the reflection signal picked up by a photodiode with large enough bandwidth. This includes a phase shifter (φ), mixer and subsequent low-pass filter (LP) which transforms the reflection signal into the PDH error signal. This is sent to a PID controller regulating the laser piezo to close the feedback loop. In addition, the error signal is viewed on an oscilloscope together with the cavity transmission signal picked up by a second photodiode. The AOM frequency is supplied by a separate signal generator and amplifier including a frequency modulation input that can also be used for the feedback signal.

3.2 Optical Setup and Electronics

The laser that is used in this work is a 1550 nm fibre laser[2] that has previously been used as part of a laser cooling setup for beryllium (similar to ref. [40]). The previous setup included a laser amplifier module that was necessary for the nonlinear optical application but that is not needed – and was therefore not used – in this work. A wavelength of 1550 nm is useful because the frequency comb that we want to lock to this laser[3] has a centre frequency of 1560 nm and therefore no extension of the comb is necessary to generate a beat note with the stabilised laser light.

[2]NKT Photonics Koheras Adjustik E15 System
[3]Toptica DFC

In section 2.2.2 we have seen the different optical and electrical elements that are needed for a PDH setup locking laser light to a stable cavity. The necessary phase modulation was performed with an electro-optical modulator[4] that was connected to a PDH module[5] which supplies the rf oscillation as well as provides the phase shifter and mixer for the processing of the reflection signal. Said reflection signal is recorded with an amplified photodiode[6] and sent to the PDH module. A PID controller[7] then sends the resulting error signal to the piezo input of the laser and hereby closes the feedback loop.

Additionally to the electrical components mentioned in section 2.2.2, an acousto-optical modulator[8] (AOM) is added in this specific setup. An AOM is used to shift the frequency of the light that passes through by the frequency of an acoustic wave, typically in the radio frequency range. In the case of the described setup, the AOM is operated at 80 MHz. Applying the stabilisation signal to modulate the AOM frequency also closes the PDH feedback loop. This potentially enables a faster feedback and will be discussed further in section 5.2. A schematic overview of the electronics setup is depicted in figure 3.4.

For the optical setup, the scheme can be seen in figure 3.5. The laser light is guided to the cavity setup by an optical fibre and passes through a fibre coupled AOM, before it is then coupled out into free space. Optical isolators prevent reflected light to go back into the fibre and damage the laser. The EOM that is used is free space, and is operated at a frequency of 8 MHz, this defines the distance of the laser's carrier frequency to the sidebands.

Together, the lens and the last two mirrors before the light reaches the resonator are used to couple the laser into the cavity.

To separate the reflected light from the incoming light and send it to the relevant photodiode, a combination of a polarised beam splitter (PBS) and a quarter waveplate is used. The laser first passes straight through the PBS, making all the traversing light linearly polarised horizontal to the laser table. For light polarised linearly at an angle of 45 deg to its fast and slow axes, a quarter waveplate changes the light's linear polarisation to a circular polarisation. After reflecting from the cavity, the polarisation of the laser is still circular, but with the opposite sense of rotation. This leads to, with a second pass through the quarter waveplate, a transformation back into a linearly polarised light beam, but this time perpendicular to the table. Therefore, the light is reflected at the PBS and can be registered on the photodiode. The polarisation of the laser light at the different positions is indicated in figure 3.5 as arrows (and dots in the case of linear polarisation perpendicular to the laser table) next to the beam path.

[4]QUBIG PM7-SWIR-1_8
[5]QUBIG ADU module
[6]Thorlabs DET20C2
[7]Toptica PID 110
[8]Gooch & Housego FIBER-Q T-M080-0.4C2J-3-F2S

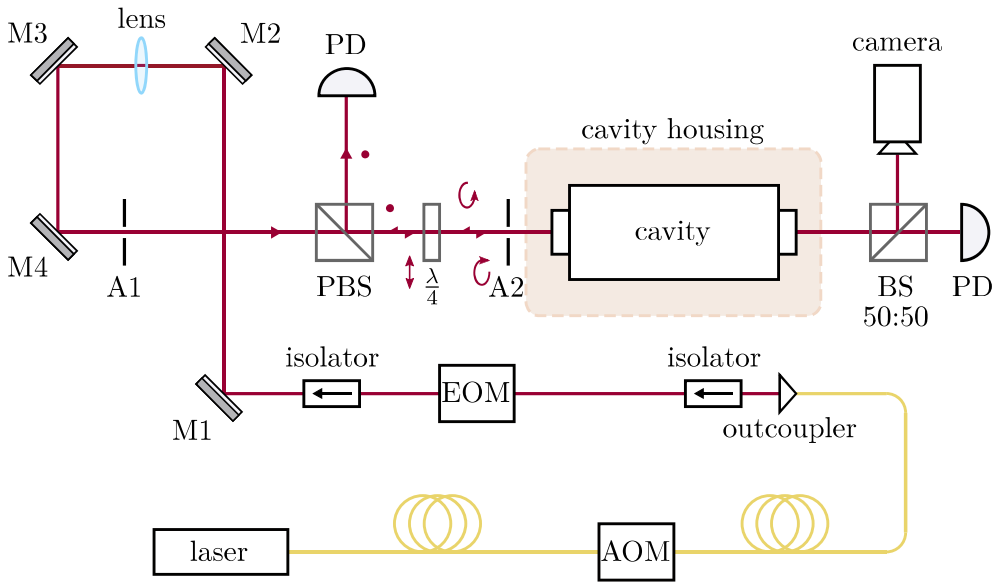

Figure 3.5: Schematic overview of the laser setup. The function of many components has already been addressed in figure 2.12. For the actual setup on the laser table, some components are added, such as an additional acousto-optical modulator (AOM) which shifts the laser frequency and can therefore also be used to apply the PDH feedback to the light. In our case this AOM is fibre-coupled and the laser enters free space subsequently. Two optical isolators have been added before and after the EOM to prevent reflected laser light to propagate back into the laser since this could damage it. Placing it after the EOM avoids etaloning effects due to the EOM crystal's reflective surface. The mirrors (labelled M) with numbers 3 and 4 are used to guide the light into the resonator, with the help of the apertures A1 and A2, while the lens ensures spatial mode overlap. The transmission can also be monitored via a camera as well as a photodiode (PD). The reflected signal is separated from the incoming light with a polarised beam splitter (PBS) and a quarter waveplate ($\lambda/4$) with the arrows next to the beam indicating the polarisation of the light; more details on this are in the text.

3.3 Improvements to the Setup

The current cavity housing already adds a degree of isolation of the cavity from the environment, but can be further improved for future operation of the setup. An important next step is to put the cavity under vacuum. As was mentioned in section 2.2.3, pressure fluctuations, especially at standard pressure, can introduce large amounts of potential noise and drifts. The housing was already built with this possibility in mind, and its design includes seals around the screws and lids.

The bronze housing already provides one degree of isolation of the resonator from the environment. The points of contact from the mounting to the cavity spacer is through viton rings on the mounting pins, making temperature changes through conduction at this point negligible, however, temperature fluctuations can still affect the cavity through radiative heat transfer from the housing and conduction through the air. It is therefore of interest to add more temperature control and insulation to the setup, while putting the cavity under vacuum would remove one mode of heat transfer. An additional insulation layer has recently been built to cover the bronze structure, protecting it from radiatively transmitted heat. However, the conduction cannot be disregarded here, as this frame remains mounted onto the laser table. A second heat shield encompassing the whole structure could be a future solution to improve upon this [54].

The permanent addition of a camera – used when coupling light into the resonator by observing the spacial mode – was made recently. Previously, a camera to monitor the transmission had been temporarily available on loan. After it was used for the first successful incoupling (details on this in the following chapter), the alignment had to not be changed again. Hence, this did not allow for changes that would impact the laser setup or move the resonator, including setting up a vacuum system and changing the cavity housing.

The positions of the mounting holes already ensure that the mounting is as insensitive to external vibrations as possible, but further improvements can be made if the cavity spacer or its mounting are passively or even actively isolated from external vibrations. Passive isolation consists of mechanical frequency filters like springs, this is already somewhat included in the design of the pins themselves due to the viton's elasticity but can be extended to include their shape (see [53]). This becomes especially important to consider once the setup is connected to vacuum pumps which can add a lot of new external perturbations, unless after the initial pumping, for continuous operation, a pump with no moving parts is chosen (e.g. an ion getter pump).

4 Incoupling and Mode-Matching

This chapter begins in section 4.1 with describing the alignment of the laser with the resonator to couple the fundamental Gaussian mode into the cavity. Afterwards, the frequency calibration of the intensity signals from scans over the laser frequency, captured with photodiodes on an oscilloscope, is detailed in section 4.2. Finally, in section 4.3 some of the transmitted intensity signals are examined.

4.1 Fundamental Cavity Mode and Laser Alignment

As a first step, the beam parameters of the fundamental transversal cavity mode need to be determined. Matching the incoming laser beam to these specifications ensures a good and efficient incoupling into the resonator. As seen in section 2.2.1, specifically in equations (2.34) to (2.36), the spatial dimensions of the fundamental mode are fixed by the cavity geometry.

In our setup we have a planar-spherical cavity, with the more detailed specifications described in the previous chapter. The cavity's spherical mirror has a radius of curvature (ROC) R_2 of 1 m and distance 100 mm to the planar mirror. The ROC of the planar mirror is considered to be $R_1 = \infty$, which immediately simplifies the above mentioned equations to

$$z_0^2 = d\,(R_2 - d)\,, \tag{4.1}$$

$$z_1 = 0\,, \tag{4.2}$$

$$z_2 = d\,. \tag{4.3}$$

This means the Rayleigh length of the Gaussian beam needed is 300 mm. At our wavelength of 1550 nm this corresponds to a beam waist radius of 385 µm (see definition of w_0 in equation (2.20)) with the waist located at the surface of the flat mirror. On the second mirror, the beam radius is 406 µm.

The same result can be achieved with the methods using transfer matrices that were introduced in section 2.1.2. To do this, one first has to calculate the transfer matrix of the whole cavity T_c by multiplying the matrices for the two mirrors with the matrix for free space propagation in between.

$$T_\mathrm{c} = T_\mathrm{prop}(d) \cdot T_\mathrm{curved}(R_2) \cdot T_\mathrm{prop}(d) \cdot T_\mathrm{flat}\,, \tag{4.4}$$

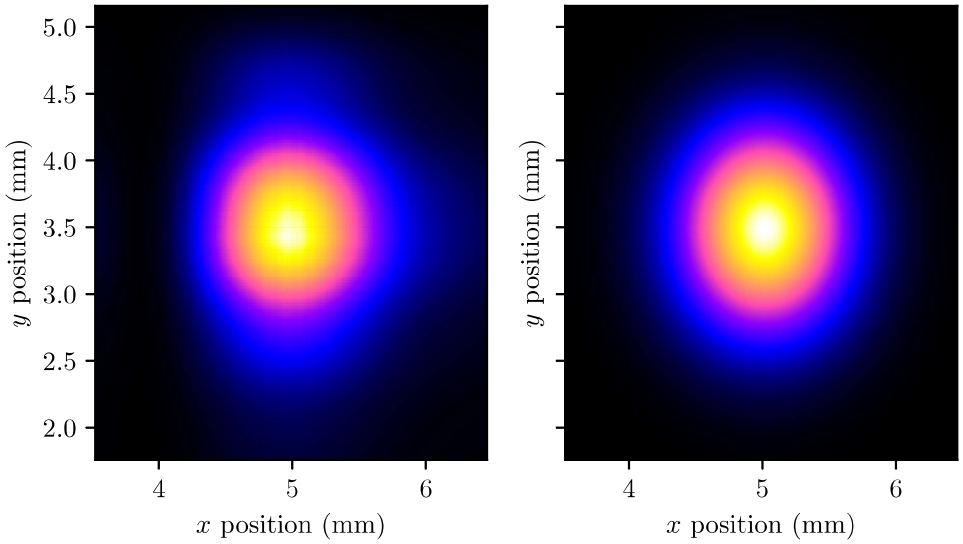

Figure 4.1: (a) Initial beam profile, measured with a beam profiler between the EOM and the mirrors used to couple into the cavity. **(b)** A 2D Gaussian fit shows a beam width of 0.897 mm in x direction and 1.087 mm in y direction which is large enough to mostly neglect the dispersion along the path of the laser on the table.

where $T_{\text{prop}}(d)$, $T_{\text{curved}}(R_2)$, and T_{flat} denote the transfer matrices for free space propagation of distance d, reflection from a curved mirror of radius R_2, and reflection from a flat mirror, respectively, according to table 2.1. To find the fundamental mode, the q-factor that is mapped onto itself has to be found. This is given by the solution to the equation

$$q = \frac{T_{\text{c},11}\, q + T_{\text{c},12}}{T_{\text{c},21}\, q + T_{\text{c},22}}\,. \tag{4.5}$$

This is a quadratic formula in q that can easily be solved, and yields

$$q = 0 + i\, 300\,\text{mm}\,, \tag{4.6}$$

which is the same result for the Rayleigh length – and therefore also the waist radius – as above. It also sets the position of the beam waist on the surface of the flat mirror.

After ascertaining the beam parameters needed to couple into the fundamental cavity mode, the optical setup that realises this beam needs to be calculated – this typically consists of an arrangement of lenses. As a first step, the initial beam has to be measured for the NIR fibre laser used here, this was done with a beam profiler[1]. The resulting profile can be seen in figure 4.1.

[1] Thorlabs BP209IR1/M

To figure out the lens with the appropriate focal length f, we can calculate its influence on the beam with the corresponding transfer matrix. For a large initial Rayleigh length – meaning a very slowly diverging beam, usually a good approximation for a free space tabletop laser setup such as we have here – the position of the beam waist can be neglected, or rather the position of the lens is taken to be at the beam waist. This means the initial q-factor can be taken as $q = iz_0$. The resulting q-factor q' is, according to the transfer matrix formalism and a lenses transfer matrix (see equation (2.25) and table 2.1, respectively), given by

$$q' = z' + iz'_0 = \frac{q}{(-1/f)q + 1} = \underbrace{-\frac{z_0^2}{z_0^2 + f^2}\, f}_{\substack{z' \\ \text{distance to new} \\ \text{beam waist}}} + i \underbrace{\frac{f^2}{z_0^2 + f^2}\, z_0}_{\substack{z'_0 \\ \text{new Rayleigh} \\ \text{length}}} . \tag{4.7}$$

For large z_0, the resulting Rayleigh length can be approximated as

$$z'_0 = \frac{f^2}{z_0^2 + f^2}\, z_0 \approx \frac{f^2}{z_0} . \tag{4.8}$$

For a given initial beam and a particular final parameter that has to be reached, the appropriate lens to achieve this has the focal length

$$f = \sqrt{z_0\, z'_0} = \frac{\pi}{\lambda}\, w_0\, w'_0 . \tag{4.9}$$

With the initial waist diameter in x and y direction $w_{0,x}$ and $w_{0,y}$ in the described setup measured as (see figure 4.1)

$$w_{0,x} = 897\,\mu\text{m} , \tag{4.10}$$
$$w_{0,y} = 1087\,\mu\text{m} , \tag{4.11}$$

and the waist of the fundamental cavity mode being calculated as

$$w'_0 = 385\,\mu\text{m} , \tag{4.12}$$

the lens that has to be used for spatial incoupling has a focal length of

$$f_x = 700\,\text{mm} , \tag{4.13}$$
$$f_y = 848\,\text{mm} , \tag{4.14}$$
$$f = 774\,\text{mm} . \tag{4.15}$$

For the last value, the average of the values calculated with the two different initial beam widths was taken. A lens of focal length 750 mm, the closest to the needed value that was acquired, was put into at the appropriate distance (starting with the focal length of the lens and later optimising the positioning for the most efficient incoupling) to the cavity into the setup. The difference in beam radius in x and y direction is not very large

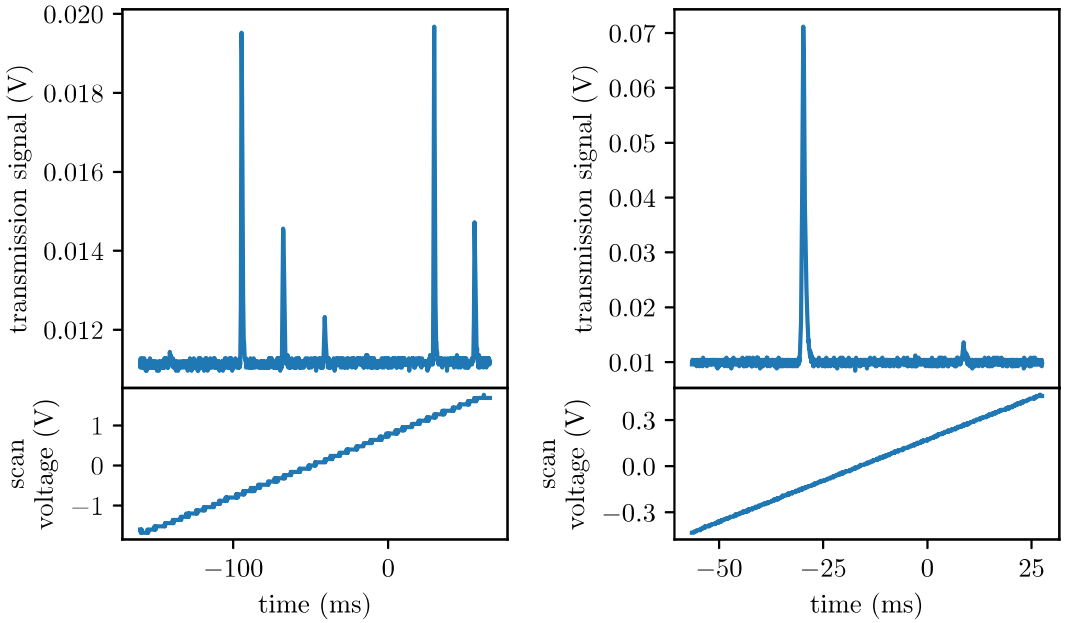

Figure 4.2: Some of the first transmitted intensity signals observed with a photodiode after the cavity. The distance of the peaks to each other cannot be derived from these figures alone, the calibration between the (monitor) scan voltage and frequency difference is described in the text and the results can be seen in figure 4.4. Varying the AOM frequency and observing the shifts immediately revealed the mode distances to be much smaller than the FSR.

and should not majorly impede the incoupling, however, if one wants to correct this it, a cylindrical lens can be added to the setup.

Spatially overlapping the incoming laser beam with the fundamental Gaussian mode also involves moving the beam to the right position and propagation direction. First, add two apertures, directly in front of the cavity, and the furthest distance possible on the laser table before reaching a mirror (they are indicated in figure 3.5) with the central position matching the cavity axis. This is done by aligning the resonator axis with a line of threaded holes on the laser table and measuring the height of its central axis. The apertures are fixed to this height and their posts are directly screwed onto the table along the chosen line.

Aligning the laser beam to the apertures can already give rise to some transversal modes being visible in the transmission signal through the cavity if the laser is scanned over a large enough frequency range (ideally more than a FSR). If no transmission is visible, then the next step consists of overlapping the incoming with the reflected beam along their shared beam path.

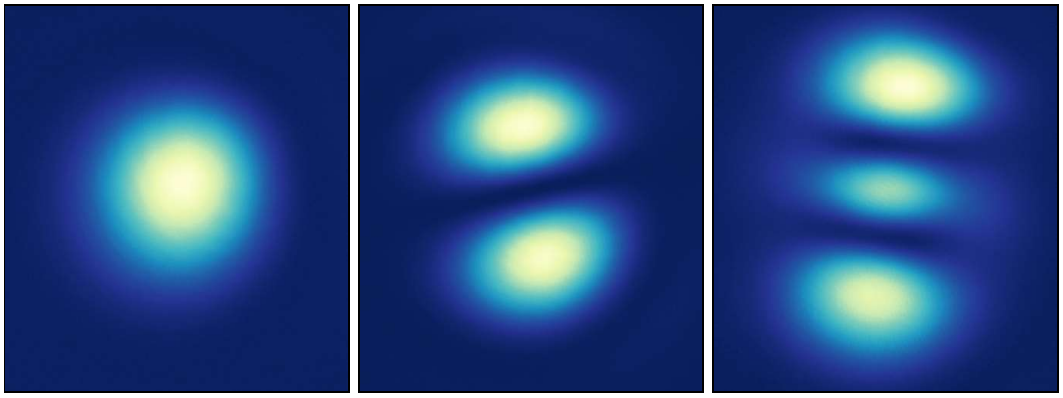

(a) (b) (c)

Figure 4.3: Pictures taken with a SWIR camera behind the cavity. The pictured lowest order modes are the ones that can still be seen after optimising the incoupling for the fundamental mode. During the optimisation process many modes of much higher orders could be observed. **(a)** Fundamental mode TEM_{00}, **(b)** TEM_{01}, **(c)** TEM_{02}. It should be noted that due to the rotational symmetry of the resonator, all orientations of higher modes of the same total order (including rotationally symmetrical ones such as 'donut' modes) couple into the cavity at the same frequency and can be observed on the camera interchangeably in no particular order or pattern.

In figure 4.2 we can see an example of the expected first transmission signal visible on an oscilloscope. The scan over the frequency was performed via the piezo of the laser and a laserlock module[2]. The transmitted signals on the photodiode do not have sufficient information to determine the number of the different modes, the only information is how well they can be coupled in, i.e. how high their transmission signal can be made to be. We expect the fundamental 00 mode to have largest possible transmission due to it having the largest mode overlap with the incident beam. If the incoupling has to be done with just this information, then one has to strategically optimise the transmission of different peaks, using the incoupling mirrors, until one is found where the transmission peaks at least twice (typically even more) as high as other peaks, and where most higher order modes vanish.

For high-finesse cavities this can be challenging, and it was in fact not possible to find the fundamental mode with just the information of the photodiode in our setup. What is needed in this case is the spatial resolution of the transmission with which the different order modes can be distinguished by their intensity distribution. A short wave infrared (SWIR) camera[3] was used to monitor the shape of the transmission simultaneously to the photodiode – this concurrent measurement setup was included in figure 3.5.

[2]TEM Messtechnik LaseLock 3.0

[3]For the first incoupling, the SWIR camera that was used was the svs-vistek exo990MGE which was later replaced with the Xenics Bobcat320-TE0.

Using the camera and therefore the mode information, an iterative process leads to incoupling the fundamental mode in very few steps. The transmitted modes are examined with the camera and the one of the lowest order is identified. Using the incoupling mirrors – the two last mirrors before the resonator – the transmission peak of this lowest mode measured with the photodiode is maximised. A new examination of all the transmitted modes will show modes of lower order than before. Usually, this does not have to be repeated often until the 00 mode, recognisable by the single Gaussian intensity peak, is one of the new emerging mode after optimising for a low order mode. Figure 4.3 shows some low order modes – the three lowest order modes in fact – that can be observed on the camera during this process.

The incoupling efficiency of the fundamental mode can then be optimised for a final time. During this step, it is also useful to optimise the lens position for the highest transmission.

4.2 Frequency Calibration

In the following sections, we want to view the oscilloscope data not depending on time as the raw data is saved but depending on the frequency over which the laser was scanned. This section will briefly discuss the two methods for this conversion used in the relevant plots for the rest of the chapter.

For the first method, the laser frequency was shifted with the AOM – typically running at 80 MHz, although it shows less but still good transmission at 70 MHz – and the change in positions of the peaks (with respect to the monitor voltage) was recorded. The monitor voltage, proportional to the scan voltage output connected to the laser piezo, was recorded as well, the peak position along this scanned voltage is the value depicted in figure 4.4. Therefore, to apply this conversion to a dataset, the monitor voltage needs to be recorded simultaneously.

Furthermore, this calibration needs data from different scans taken successively for each of the AOM settings. As we observe frequent drifts of the resonance peaks, either caused by external influences/perturbations or drifts of the laser itself, successive measurements even taken quickly after one another can be distorted. Therefore, we need to choose between fewer measurements to hopefully prevent too much drifting between them, but still taking enough for a reasonable calibration. The presented measurements were taken at 80 MHz, 75 MHz and 70 MHz and then one additional at 80 MHz to compare possible drifts.

For measurements in chapter 5, the EOM is used to introduce sidebands of a known frequency (here 8 MHz) to the laser light. If these can be observed at their shifted resonance in the same scan as the main carrier, these resonance positions can be used for the conversion. This is more convenient since this does not need separate measurements,

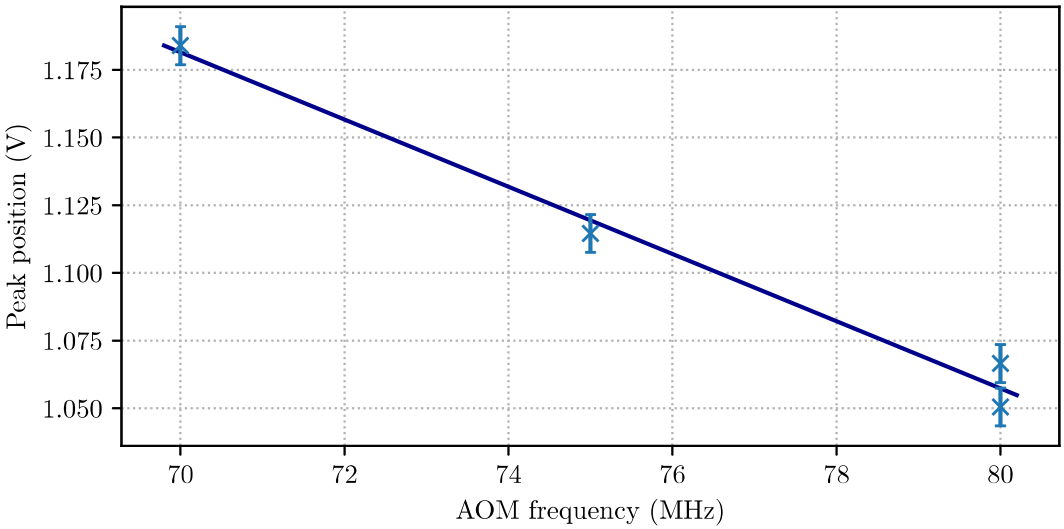

Figure 4.4: Calibration for conversion between monitor scan voltage and frequency offset. The AOM was used to change the laser frequency and the position of the resonance peak along the (monitor) scan voltage was recorded for the different values. Since separate scans for the different AOM settings are necessary, the drifts of the resonance peaks that are observed (often larger than the shifts recorded here due to the AOM frequencies) can distort the calibration. Hence only a small number of frequency points were taken to minimise the time of the measurements. The first and last scan were both taken at 80 MHz to get a measure of the size of the shift during the measurement. As we can see in the figure, there seems to have been a small drift during the successive measurements but they still agree well enough to fit a calibration line. The error bars stem from the position of quite noisy resonance peaks.

which largely eliminates the effect of the drifts. On the timescale of a single scan, they can be neglected.

4.3 Transmitted Intensity Signals

In figure 4.5, the transmission signal on the photodiode of the lowest three modes (the TEM00, TEM01 and TEM02 depicted in figure 4.3) can be seen. The distance of their resonance frequencies seems to be equidistant. In fact, from this graph it can be measured to be

$$\Delta\nu_{00,01} = 143.9(3)\,\mathrm{MHz}\,, \tag{4.16}$$

between the TEM_{00} and the TEM_{01} modes and

$$\Delta\nu_{01,02} = 144.9(3)\,\mathrm{MHz}\,, \tag{4.17}$$

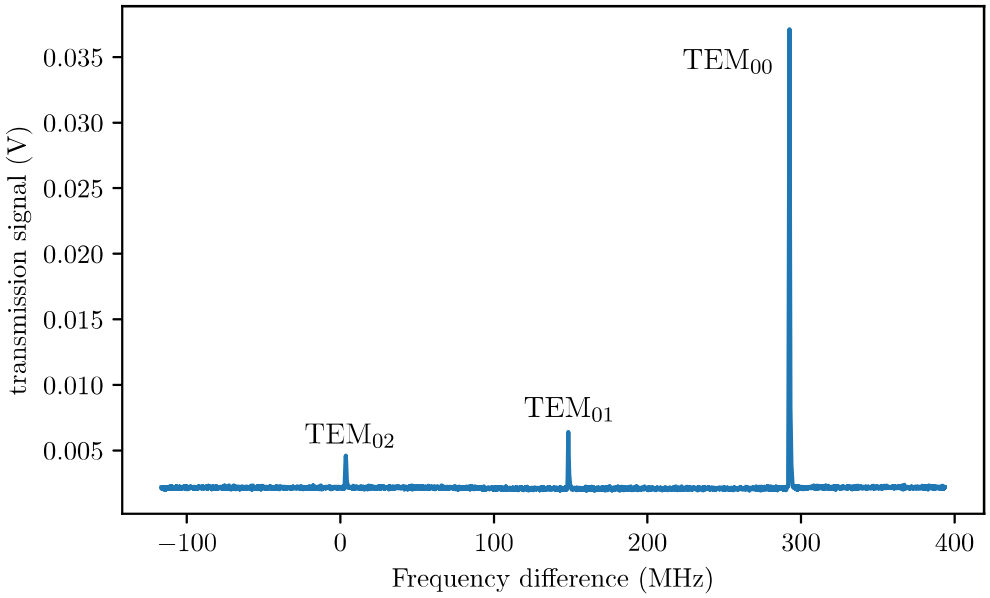

Figure 4.5: Transmission after optimising for the fundamental 00 mode which corresponds to the highest peak in the figure. The neighbouring peaks are the first and second order modes, their intensity distributions are depicted in figure 4.3. One can notice the equidistant spacing of these modes to each other, this is described by the transverse mode spacing ν_{TEM} (see equation (4.18)).

between the TEM_{01} and TEM_{02} modes.

The difference in frequency between neighbouring modes is described by the so called transverse mode spacing ν_{TEM} and stems from the added phase component for higher modes that emerged in equations (2.29) and (2.30) [55]. This value depends on the free spectral range ν_{FSR}, and the Gouy phase shift φ_G that is gained per round trip for higher modes.

$$\nu_{\mathrm{TEM}} = \nu_{\mathrm{FSR}} \frac{\varphi_G}{2\pi} . \tag{4.18}$$

Therefore, this spacing can also be derived from the geometrical properties of the resonator since this sets constraints on the modes that build up in the resonator.

To characterise the Gouy phase shift for the cavity used here, we first have to regard the Gouy phase acquired by the fundamental mode between positions $z_1 = 0$ and $z_2 = d$ of the mirrors:

$$\varphi_G(z_1 \to z_2) = \arctan\left(\frac{z_2}{z_0}\right) - \arctan\left(\frac{z_1}{z_0}\right) = \arctan\left(\frac{d}{z_0}\right) . \tag{4.19}$$

For a higher mode of order (l, m) the Gouy phase obtained is

$$\varphi_{lm}(z_1 \to z_2) = (l{+}m{+}1)\, \varphi_G(z_1 \to z_2) = (l{+}m{+}1)\, \arctan\left(\frac{d}{z_0}\right) . \tag{4.20}$$

For one round trip in the resonator, this phase is doubled, making the phase difference of neighbouring (where their respective $l+m$ differs by one) modes

$$\varphi_G = 2 \arctan\left(\frac{d}{z_0}\right) . \tag{4.21}$$

With equation (4.18), this leads to an expected transverse mode spacing of

$$\nu_{\mathrm{TEM}} = 153.52\,\mathrm{MHz} . \tag{4.22}$$

The difference to the measured mode spacing could be caused by the shapes of the mirrors (especially their ROC) differing from the expected parameters. This changes the Gaussian beam parameters and therefore the Gouy phase, leading to a different mode spacing. The inconsistencies could also stem from errors of the frequency calibration, causing the measured values to be shifted.

Additionally, it can be observed how the transmission peaks become a lot more asymmetrical for faster scan speeds. As the frequency is swept over the resonance, the built up intensity inside the resonator leaks out over time and leads to a 'tail' in the transmission. This appears to be visible in figure 4.6. Ref. [56] offers a good description of the expected transmission signals for different scan speeds. The observed exponential tail is consistent with a cavity ringdown signal, but the observed time constant is much larger (by two orders of magnitude) than expected from our finesse. Therefore, the observed effect seems to be dominated by the response time of the detector.

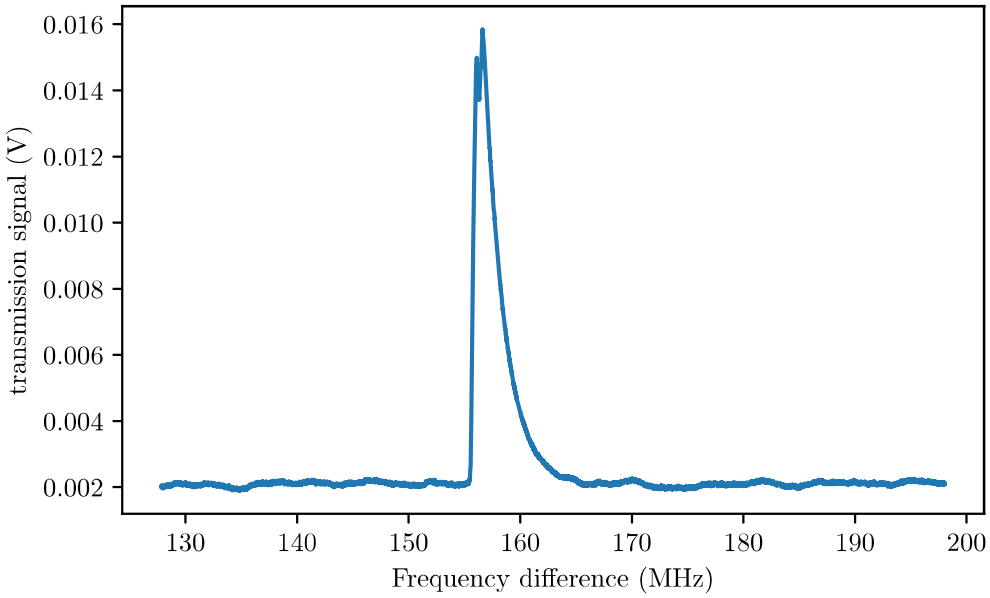

Figure 4.6: Transmitted intensity signal of the single mode at a faster scan. For a faster scan speed over the laser frequency, the transmission peaks appear broader and more asymmetrical. The reason for this asymmetry is a combination of the ring-down effect of the cavity (with the built-up light inside the resonator being stored for some time and leaking out gradually) and the response time of the combination of photodiode and oscilloscope.

5 Pound-Drever-Hall Results

This chapter presents the steps that were taken to realise the PDH locking in our setup. Initial electronic signals were exceedingly noisy, the source of which was identified as detailed in section 5.1. Section 5.2 describes the first locking attempts and gives estimates of the laser stability. Finally, section 5.3 will go over future measures that can be taken to improve the setup and increase the laser stability.

5.1 Signal Noise Investigations

The first step from the successfully coupled cavity towards the PDH setup is to add the EOM for phase modulation (see figure 3.5).

This induces frequency sidebands in the laser light and means that the PDH signal can be observed if the reflection signal is processed according to earlier discussions in sections 2.2.2 and 3.2. This first PDH signal is shown in figure 5.1 alongside the transmission signal.

The sidebands are visible in the transmission signal and the characteristic PDH error signal can be recognised, but we observe that the overall noise level in both signals is very high. In the transmission, the height of the peaks fluctuates constantly and the shape, for which we expect a Lorentzian lineshape with a potential asymmetric exponential decay due to the scan speed, also shows large amounts of noise. Fluctuations in the maximum could maybe be explained for very fast scans and undersampling by the oscilloscope, but the effects are also visible for low scan speeds.

The noise is also very visible in the PDH error signal, especially in the relevant linear segment around the resonance. It is too noisy to close the feedback loop and lock the setup, even after we tried to get a better signal-to-noise ratio by amplifying the relevant reflection signal. This did not have the desired effect and the reflection signal as well as the resulting error signal remained very noisy.

Instead of the biased photodiode with separate signal amplification used initially, we chose to implement a new amplified photodiode[1]. We expect a better signal-to-noise ratio and indeed we see an improvement, but it is still very noisy and not good enough to engage the lock. The amplifier from before used together with this new photodiode did also not improve the signal noise.

[1] Thorlabs PDA05CF2

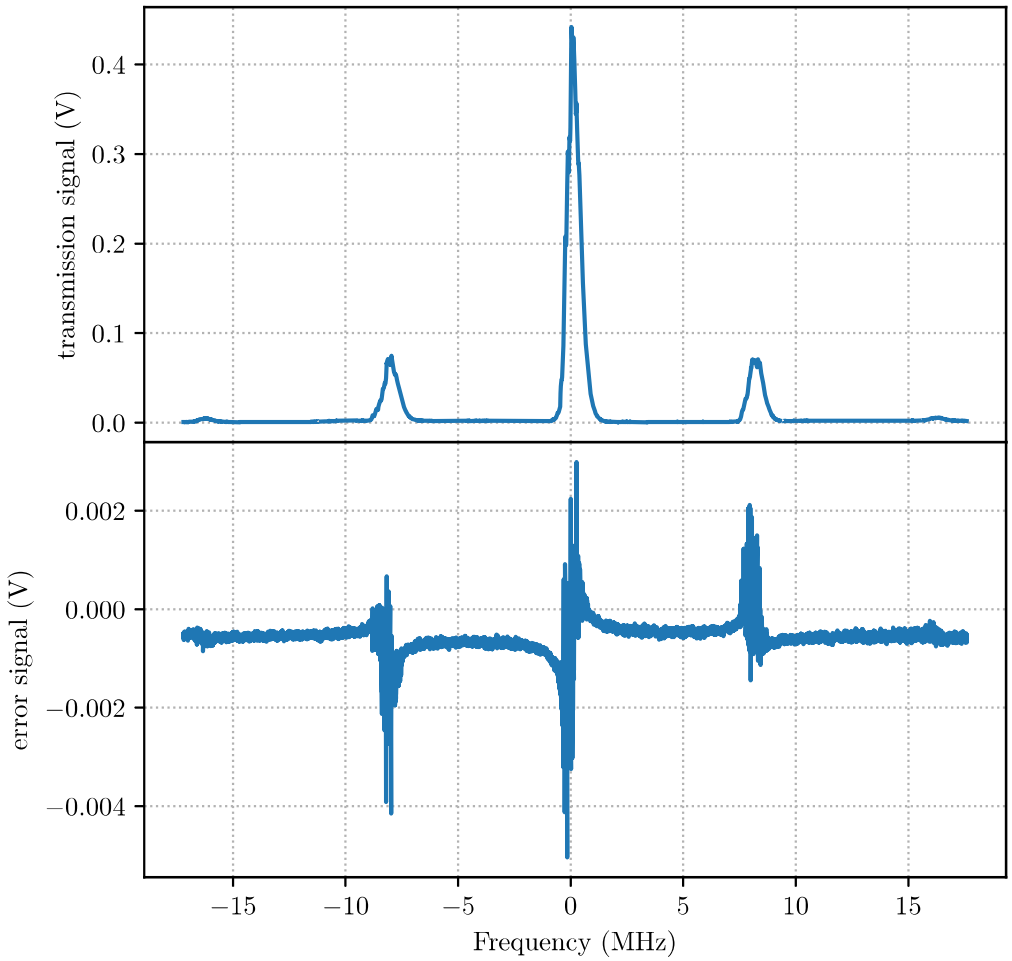

Figure 5.1: Initial transmitted intensity and the simultaneously measured PDH error signal of the phase-modulated light of the fundamental resonator mode. The sideband power is about 15 % of the carrier power, corresponding to a modulation depth β of about 0.7, see equations (2.59) and (2.60), and the second sidebands at twice the modulation frequency are only just visible. The error signal, and especially the linear slope at the resonance, is very noisy such that a stable lock will not be possible. Subsequent changes to the setup that improved the signal are discussed in the text.

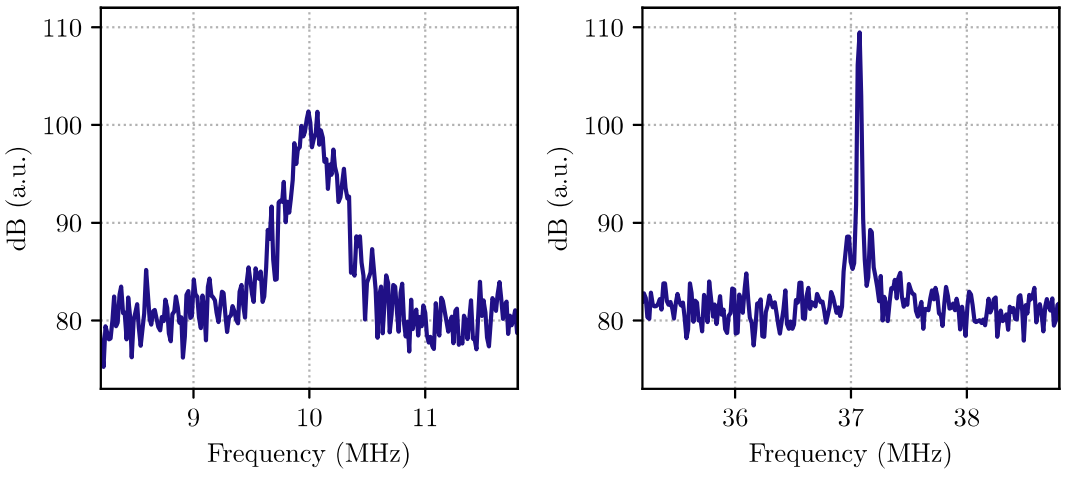

Figure 5.2: Two different beat notes between the free-running fibre laser and the frequency comb. **(a)** During this measurement the laser piezo modulation input was connected to the TEM Messtechnik lockbox that had been used for all the scans this far, and that also has locking capabilities. However, the FWHM of this beatnote is approximately 250 kHz which is larger than expected from the laser and comb linewidths. **(b)** This beatnote sigal was measured when the input to the laser piezo was turned off. An immediate improvement to the one before is evident and the FWHM is now about 20 kHz. There was no observable change in the shape and width of the beatnote when connecting a new module, this time the Toptica PID 110.

As a new approach, the laser light was investigated with the frequency comb by forming a beat note. The frequency comb in our lab has a spacing of 80 MHz, so the furthest the laser frequency can be from a comb tooth is 40 MHz and there is always a beatnote between 0 MHz and 40 MHz. Since our laser, according to its specifications, already has quite a narrow linewidth, we expect a narrow beat note with the frequency comb. However, what we saw was a very noisy and wide beatnote, depicted in figure 5.2a, with a FWHM of about 200 kHz to 250 kHz, which is much larger than expected. More importantly, it is larger than beatnotes between the frequency comb and other lasers, therefore the observed noise is caused by our fibre laser.

Eventually, we found that a main cause for the noise is the lockbox that was used to drive the piezo input of the fibre laser, which was still connected while the beatnote was measured. With this device switched off or removed we obtained a more narrow beatnote which can be seen in figure 5.2b. Here, the FWHM is about 20 kHz, already an order of magnitude better than before.

A different PID box[2] was used to supply the electric signal to the laser piezo following this

[2]Toptica PID 110

discovery. It was confirmed that no additional noise was added by this new component; no broadening of the beatnote was observed when connecting this module.

The resulting transmission, reflection, and PDH error signals can be seen in figure 5.3. It is immediately apparent that the noise levels have drastically improved.

A cleaner reflection signal also means we now give a value for the incoupling efficiency. However, the reflection signal in figure 5.3 looks different than anticipated. What we expect is the opposite of the transmission, with a constant value for all the reflected light for most of the scan and Lorentzian shaped dips in the intensity at the carrier and sideband resonances. Instead, if we zoom into the reflection signal (see figure 5.4) around the resonance, we see oscillations in the signal.

These oscillations can be explained by interference effects when scanning the laser frequency across the resonance of a high-finesse cavity [56]. When the scan reaches the resonance frequency, intensity builds up inside the resonator, is stored for some time (the ringdown time) and gradually leaks out. All the while, the frequency scan continues to off resonance frequencies which are totally reflected without entering the resonator. Hence, the light that is directly reflected is superimposed with light leaking from the cavity. This causes a beating on the observed signal since the immediately reflected light will be frequency shifted due to the scan with respect to the on-resonance light leaking from the resonator. Additionally, due to the finite cavity linewidth, light of different frequencies enters the cavity, leading to interferences that would be visible in both the reflection and the transmission signal (in the latter it is likely obscured by the detector response).

The observed oscillations therefore depend on the scan speed. Since this is a phenomenon that only shows up because of the frequency scan, it will not impact the locking performance.

Using the description of the electric fields during a frequency sweep in [56] qualitatively similar oscillating behaviour in reflected signals could be reproduced. Depending on scan parameters, the interference also alters the depth and width of the on-resonance dip in reflected intensity. Even for a lossless perfectly aligned cavity where the reflection resembles an inverted Lorentzian for a vanishing scan speed, the signal becomes wider and the dip less deep.

Therefore, the minima of the measured signal can still be used to give a lower bound for the incoupling efficiency ε. At off-resonance frequencies, the measured reflection signal is

$$V_{\max} = 434(1)\,\mathrm{mV}, \tag{5.1}$$

which corresponds to the carrier intensity I_c and twice the sideband intensity I_s.

$$V_{\max} = \alpha(I_\mathrm{c} + 2I_\mathrm{s})\,, \tag{5.2}$$

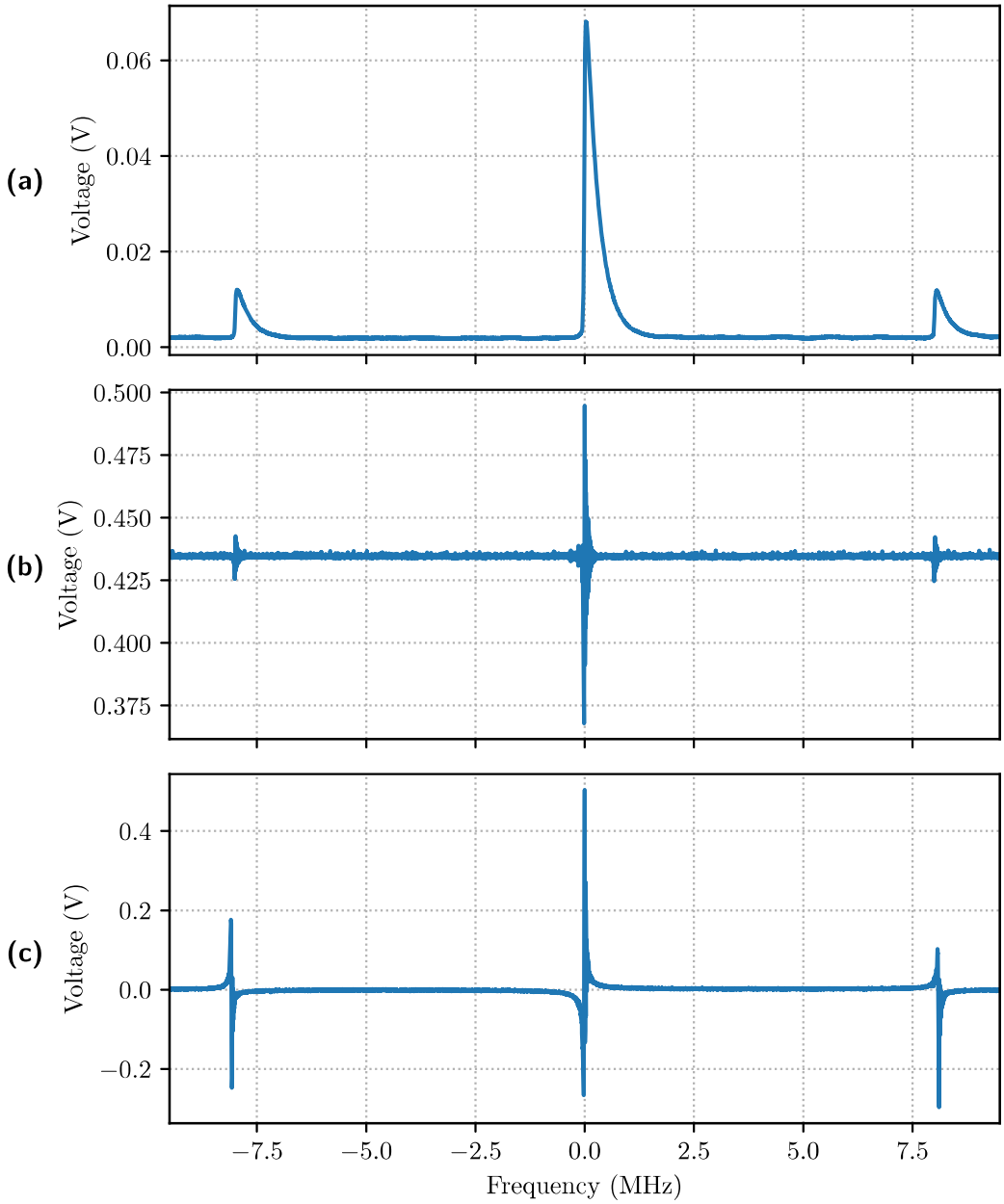

Figure 5.3: Signals of the transmission, reflection and the PDH error signal with improved noise levels after switching to a new lockbox. In comparison to the signals in figure 5.1, a large improvement is obvious. **(a)** The shape of the transmitted intensity peaks is a lot cleaner than before, they appear more asymmetrical due to the faster scan speed of the new module, this asymmetry still being dominated by the detector effects. **(b)** The expected reflection signal is an inverted Lorentz curve which is not what we can observe here. Additional oscillations, better resolved and explained in more detail in figure 5.4, alter the signal. **(c)** Since the PDH error signal is derived from the reflection signal, the oscillations mentioned above are also observed here. They can be explained by effects from the frequency scan which means that they will not impact the locking performance.

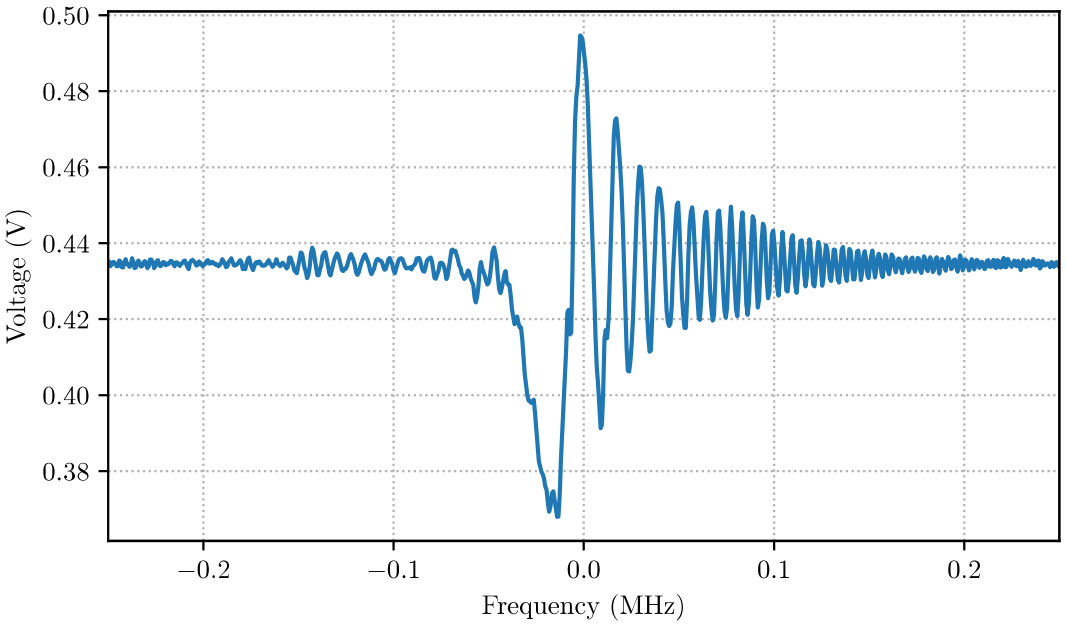

Figure 5.4: A closer look at the reflection signal of the carrier resonance from figure 5.3, taken after the noise level of the setup was improved. The oscillations are visible after the initial expected dip in intensity when reaching the resonance frequency. This can be explained by interference of light directly reflected from before entering the cavity and light leaking from the cavity after some power has built up at resonance. While the directly reflected part has a frequency according to the moment in the scan, the light leaking from the resonator fulfills the resonance condition. This difference leads to a beat signal that is visible here. More information on the reflection shape can be found in the text. We still calculate a value for the incoupling efficiency from this signal. Typically, if the reflection signal vanishes at the resonance, then the incoupling efficiency is 100 %, but for one, the sidebands contribute to the total intensity and are always reflected at the carrier resonance, and second, the oscillations alter the signal, including reducing the depth of the minimum. Therefore, the observed dip in the intensity gives a lower bound of 19.3(7) % for the incoupling efficiency.

where α describes the detector efficiency. The signal decreases to

$$V_\mathrm{c} = 368(1)\,\mathrm{mV} \tag{5.3}$$

at the carrier resonance and to

$$V_\mathrm{s} = 425.2(4)\,\mathrm{mV} \tag{5.4}$$

at the sideband resonances. At each of these frequencies, only a fraction of the laser light according to incoupling efficiency is coupled into the resonator, and only the part of it fulfilling the resonance condition. This means

$$V_\mathrm{max} - V_\mathrm{c} = \alpha\varepsilon I_\mathrm{c}\,, \tag{5.5}$$
$$V_\mathrm{max} - V_\mathrm{s} = \alpha\varepsilon I_\mathrm{s}\,. \tag{5.6}$$

Together with equation (5.2) the minimum incoupling efficiency follows as

$$\begin{aligned}\varepsilon &= \frac{V_\mathrm{max} - V_\mathrm{c} + 2V_\mathrm{max} - 2V_\mathrm{s}}{V_\mathrm{max}} \\ &= 19.3(7)\,\%\,.\end{aligned} \tag{5.7}$$

The actual incoupling efficiency is likely higher due to the aforementioned reasons.

5.2 PDH Locking and Stability Estimates

With the cleaner and less noisy signals after switching to better electronics, it was possible to enable the feedback loop with the PID controller to engage the lock. For a good lock, we expect the monitored error signal to vanish and to stay at 0 and only move around it a little as the feedback loop counteracts small variations. Similarly, we expect the transmission to go to a maximum and stay there at a relatively constant value. Typical signals we observe when the lock engages after optimizing the PID parameters can be seen in figure 5.5. The continuously transmitted intensity indicates a successful lock, but the fluctuation in intensity and deviation of the error signal from zero show that the feedback loop is unable to fully compensate perturbations.

During this measurement, the feedback loop is connected to the piezo input of the laser. A reason for the high noise level could be that the speed of the modulation feedback (the modulation bandwidth) is not quick enough to counteract the frequency noise broadening the laser. According to fibre laser's specifications the maximum modulation bandwidth of the piezo input is 20 kHz. This might be too slow for our purposes.

Instead of the fibre laser piezo, it is also possible to use the AOM to control the laser frequency (see figure 3.4), to potentially reach a significantly higher feedback bandwidth; the limit for the frequency modulation of the oscillator driving the AOM is 7 MHz which

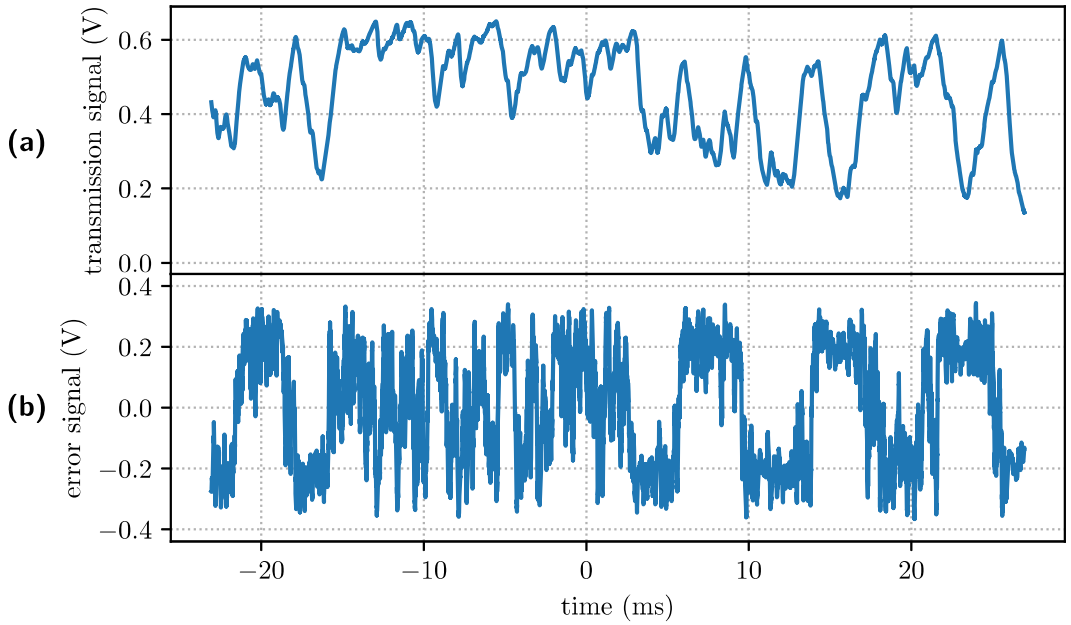

Figure 5.5: Observed signals for an enabled lock. **(a)** Here, the transmitted intensity is depicted while the PDH feedback loop is closed. Instead of reaching a maximum and constantly staying there, the intensity fluctuates to less than half the peak value it reaches. **(b)** The error signal is expected to stay at 0 for a successful lock, with only small fluctuations and potential regular oscillations in case the lock is too strong. What we see is a lot more noisy, as there seem to be noise components that the feedback loop cannot compensate, or too many external perturbations. The amplitude of the rather large fluctuations of the error suggest a change in the resonance frequency of the order of 10 kHz.

should be sufficient. However, when we engage the lock this way we get similar results to the ones pictured in figure 5.5.

The bandwidth of the PID module could also be insufficient as it has a limit of 100 kHz. Therefore, we plan to switch to a Toptica FALC lockbox instead in the future. This module has a modulation bandwidth of up to 50 MHz.

Instead of a lacking modulation bandwidth, the stability of the lock could also be held back by the length stability of the resonator. The amplitude of the fluctuations in the error signal in figure 5.5 suggests short-term instabilities of the order of 10 kHz. This corresponds to a fractional instability of 10^{-11}. On longer timescales of tens of seconds to minutes, frequency drifts of hundreds of kHz to MHz could be observed which equals a fractional uncertainty on the 10^{-9} level.

In the following, there will be an overview of how we expect the external perturbations discussed in section 2.2.3 to impact the fractional instability, whether they might be responsible for the observed instabilities and on what level they should be controlled for

optimal performance. For this, we consider the optimal performance to be at a linewidth and stability uncertainty of about 1 Hz which is what the frequency comb can reach when locked to a stabilised laser. This means the fractional frequency instability has to be reduced to the order of 10^{-15}. Setups with similar ULE cavities have reached below the 10^{-16} level [54].

First, we want to take a look at the impact of temperature instabilities. As discussed in section 3.1, the coefficient of thermal expansion of the cavity is expected to be on the order of $10^{-7}\,\mathrm{K}^{-1}$. Length changes caused by a shift in temperature contribute to instabilities on longer timescales and are not likely a reason for the fast noise observed in figure 5.5. However, the observed slow drifts on the order of 10^{-9} would translate to temperature changes of 10 mK. Even though we have a temperature shielding, this could be plausible. The housing is mounted on the laser table and is only protected from radiative heat transfer, not conductive transfer through the table. The cavity spacer is subject to both radiative and conductive heat transfer through air from the housing. The influence is often quantified with the thermal response time which is ideally made as high as possible to filter away fast temperature fluctuations and reduce the rate of length change.Often, several heat shields are used to achieve this which can lead to thermal response times of the order of hours or even days. Some rough estimations suggest that in our case the heat transfer to the cavity is dominated by thermal conduction through the air and the thermal response time is not more than two hours.

In equation (2.68) and ref. [49] we have seen that a change in pressure ΔP is proportional to the fractional instability. For the fast instabilities on the order of 10^{-11} this would correspond to pressure fluctuations of $4 \cdot 10^{-5}$ mbar over a short period of time. On slightly longer timescales, the expected fluctuations at atmospheric pressure are on the order of 10^{-4} mbar per second. Therefore, it is possible that the noise we see in figure 5.5 is dominantly caused by pressure fluctuations. The observed slow drifts could be explained by slow pressure changes around $4 \cdot 10^{-3}$ mbar, which is very plausible. Since the fractional frequency instability scales with absolute pressure changes, putting the resonator in a vacuum should show an immediate improvement. If the fractional pressure fluctuations stay the same, even a medium vacuum of 10^{-1} mbar to 10^{-2} mbar could be enough to reach the desired fractional uncertainty of 10^{-15}. In case pumping leads to larger fluctuations, it is desirable to go to lower pressures.

External vibrations can cause deformations in the cavity spacer that change the length. The relevant vibrations that cause this effect are slower than 100 Hz. Typically, most mountings of ULE spacers show a vibration sensitivity on the order of $100\,\mathrm{kHz}/(\mathrm{m/s^2})$. For a cavity with very similar parameters (length and material) and mounting configuration (optimised position of mounting holes) to ours, the vibration sensitivity was measured to be $1.5\,\mathrm{kHz}/(\mathrm{m/s^2})$ and $14\,\mathrm{kHz}/(\mathrm{m/s^2})$ in the vertical and horizontal directions, respectively [53]. This would correspond to a fractional frequency sensitivity between $10^{-10}\,(\mathrm{m/s^2})$ and $10^{-12}\,(\mathrm{m/s^2})$. In a quiet laser lab we expect less than $10^{-3}\,\mathrm{m\,s^{-2}}$ vibrations which would then lead to fractional uncertainties between 10^{-13} and 10^{-15}. This already seems better than the perturbation effects addressed above and it would

mean that this is not the cause of the observed noise level. Once the other potential noise sources are taken care of, this can be revisited, and measurements and simulations can be made to characterise the vibration sensitivity further.

The build-up of large intracavity intensities leading to localised heating and length changes, as well as effects from residual amplitude modulation are less relevant for the current locking circumstances and will therefore not be discussed here. Once the lock is more stable they will become more significant and will have to be considered.

5.3 Future Measurements

Once the lock engages and provides a stable transmission and error signal, some further measurements can be taken.

A cavity ring-down measurement can be done once the lock is stable. When the laser is locked, the laser power is turned off abruptly (e.g. using the AOM) and the exponential decay in the transmitted intensity yields a value for the lifetime of the light in the resonator. From this value, the finesse can be calculated, which should give a more accurate value than the lower limit specified from the manufacturing.

Once the lock engages and is stable, we want to quantify the laser linewidth and its improvement with the PDH lock. To get linewidth measurements, one ideally uses a second narrower or equally narrow laser source of the same wavelength and analyses the beatnote. The setup described in this thesis in the first laser in our lab to be stabilised by a cavity, but there may be a chance to measure it against a cavity-stabilised one being assembled as part of a project in a different division.

Alternatively, one could employ the technique of self-heterodyne detection, where the laser source is referenced against a frequency-shifted part of itself to get a measure of its linewidth [57]. To ensure that the noise in the two beams is uncorrelated, one of them is sent through a long optical delay-line fibre. Such a fibre has already been ordered and should soon be available for this application.

6 Conclusion and Outlook

Within the scope of this work, a PDH frequency stabilisation laser system was set up and a first closed feedback loop was characterised. It is built for the goal of performing high precision spectroscopy on highly charged ions by locking a frequency comb, which can be used for referencing different spectroscopy lasers, to the stabilised fibre laser operating at 1550 nm. While the current locking signals suggest a large amount of noise that prevents this step, the areas where improvements are needed to reach it, have been identified.

The assembly of the setup had different parts, starting with the mounting of the cavity. The cavity itself consist of a 10 cm ULE spacer with optically contacted silicon mirrors at both ends. A bronze housing was designed and built which acts as a shield against short-term temperature fluctuations. It also holds the pins that hold up the ULE cavity spacer, their positions and those of the mounting holes being optimised for minimal length changes through external vibrational perturbations. The chamber was already constructed with the potential for a future vacuum system in mind. It is not under vacuum yet because we had a short window of time for the coupling of the laser beam into the cavity and it was not possible to move the cavity after this step.

This incoupling of the laser beam consisted of two parts. The laser beam's wavefronts need to match the surfaces of the cavity mirrors, to reach the correct Gaussian beam parameters a lens is used. It was calculated that in our case, with an averaged initial beam radius of 992 µm, a lens with a focal length of approximately 750 mm was needed to match the resonator mode.

To overlap the incoming laser beam with the cavity axis two mirrors were used to adjust the pointing. The better the overlap the more power is coupled into the fundamental mode of the resonator; for slight misalignments, higher cavity modes might be excited instead. After some initial trial and error using the total transmitted intensity as a guide for the alignment process, it was evident that a camera to monitor the spatial intensity distribution of the transmission is necessary (at least for a high finesse cavity such as we have here). Monitoring the cavity modes on the camera, the alignment became an iterative procedure of finding the lowest order visible across the frequency spectrum and changing the alignment for the highest possible intensity of this mode. Finally, a lower limit for the incoupling efficiency of the fundamental resonator mode that was achieved was determined to be 19.3(7) %.

Once the fundamental resonator mode was incoupled successfully, issues with excessive noise in electronic signals became apparent and had to be fixed. We observed that the transmission signal did not resemble a Lorentzian shape very well, and the error signal

was too noisy to enable the PDH lock. By taking beat note measurements between our (free-running) fibre laser and the frequency comb and seeing that it was also showing a large amount of noise, we knew that the problem could not concern the resonator. The source for the majority of the noise could be identified as the electronic lockbox connected to the piezo input of the laser. After replacing this part, the beatnote showed improvement, and expected levels of noise.

With this modification, the electronic signals of the PDH setup were also a lot less noisy, and the feedback loop could be enabled. The remaining noise and drifts visible in the locking signal were estimated to be at a fractional frequency instability of about 10^{-11} and 10^{-9}, respectively. On the one hand, the possible improvements to reduce these levels include upgrading the locking electronics to increase the feedback modulation bandwidth. At the moment, this is limited to 100 kHz by the PID module which might not be high enough to counteract higher frequency contributions to the laser noise spectrum.

On the other hand, it is possible for the observed noise and drift to be caused by instabilities of the reference resonator. Influences of different sources of external perturbations on the cavity were estimated. Fluctuations of the temperature can induce a length change of the cavity spacer which could be the cause of the drifts that we see on the order of seconds and minutes. Changes in pressure might be responsible for the faster noise that was observed, as well as some drifting on longer timescales. In our estimations, external vibrations causing length changes were less significant, but once the setup has been improved concerning the two previous issues, it should be possible to give a better estimation of this.

Since operating the cavity in vacuum has been foreseen in the design, it will be straightforward to implement and reach at least a low vacuum. Additionally, electronics suitable for setting up a higher bandwidth feedback loop are available to replace the ones currently in use. Along with the other steps sketched in this work, this is expected to bring significant improvements to the achieved stability in the near future.

Bibliography

[1] T. H. Maiman, 'Stimulated optical radiation in ruby', Nature **187**, 493–494 (1960).

[2] D. Browne, S. Bose, F. Mintert and M. Kim, 'From quantum optics to quantum technologies', Progress in Quantum Electronics **54**, Special issue in honor of the 70th birthday of Professor Sir Peter Knight FRS, 2–18 (2017).

[3] C. H. Bennett and D. P. DiVincenzo, 'Quantum information and computation', Nature **404**, 247–255 (2000).

[4] A. D. Cronin, J. Schmiedmayer and D. E. Pritchard, 'Optics and interferometry with atoms and molecules', Rev. Mod. Phys. **81**, 1051–1129 (2009).

[5] M. S. Safronova, D. Budker, D. DeMille, D. F. J. Kimball, A. Derevianko and C. W. Clark, 'Search for new physics with atoms and molecules', Rev. Mod. Phys. **90**, 025008 (2018).

[6] T. Udem, R. Holzwarth and T. W. Hänsch, 'Optical frequency metrology', Nature **416**, 233–237 (2002).

[7] J. M. Beckers, 'Adaptive optics for astronomy: principles, performance, and applications', Annual Review of Astronomy and Astrophysics **31**, 13–62 (1993).

[8] G. de Medeiros, D. Kromm, B. Balazs, N. Norlin, S. Günther, E. Izquierdo, P. Ronchi, S. Komoto, U. Krzic, Y. Schwab, F. Peri, S. de Renzis, M. Leptin, M. Rauzi and L. Hufnagel, 'Cell and tissue manipulation with ultrashort infrared laser pulses in light-sheet microscopy', Scientific Reports **10**, 1942 (2020).

[9] H. Xin, B. Namgung and L. P. Lee, 'Nanoplasmonic optical antennas for life sciences and medicine', Nature Reviews Materials **3**, 228–243 (2018).

[10] H. Al-Taiy, N. Wenzel, S. Preußler, J. Klinger and T. Schneider, 'Ultra-narrow linewidth, stable and tunable laser source for optical communication systems and spectroscopy', Opt. Lett. **39**, 5826–5829 (2014).

[11] J. Fraunhofer, 'Bestimmung des brechungs- und des farbenzerstreungs-vermögens verschiedener glasarten, in bezug auf die vervollkommnung achromatischer fernröhre', Annalen der Physik **56**, 264–313 (1817).

[12] G. Kirchhoff and R. Bunsen, 'Chemische Analyse durch Spectralbeobachtungen', Annalen der Physik **189**, 337–381 (1861).

[13] D. J. Wineland, R. E. Drullinger and F. L. Walls, 'Radiation-pressure cooling of bound resonant absorbers', Phys. Rev. Lett. **40**, 1639–1642 (1978).

[14] K. Zhao, Q. Zhang, M. Chini, Y. Wu, X. Wang and Z. Chang, 'Tailoring a 67 attosecond pulse through advantageous phase-mismatch', Opt. Lett. **37**, 3891–3893 (2012).

[15] T. Udem, J. Reichert, R. Holzwarth and T. W. Hänsch, 'Absolute optical frequency measurement of the cesium D_1 line with a mode-locked laser', Phys. Rev. Lett. **82**, 3568–3571 (1999).

[16] T. W. Hänsch, 'Nobel lecture: passion for precision', Rev. Mod. Phys. **78**, 1297–1309 (2006).

[17] A. A. Michelson and E. W. Morley, 'On the relative motion of the earth and the luminiferous ether', American Journal of Science **s3-34**, 333–345 (1887).

[18] B. P. Abbott et al., 'LIGO: the Laser Interferometer Gravitational-Wave Observatory', Reports on Progress in Physics **72**, 076901 (2009).

[19] A. D. Ludlow, M. M. Boyd, J. Ye, E. Peik and P. O. Schmidt, 'Optical atomic clocks', Rev. Mod. Phys. **87**, 637–701 (2015).

[20] C. Eisele, A. Y. Nevsky and S. Schiller, 'Laboratory test of the isotropy of light propagation at the 10^{-17} level', Phys. Rev. Lett. **103**, 090401 (2009).

[21] S. Bize et al., 'Cold atom clocks and applications', Journal of Physics B: Atomic, Molecular and Optical Physics **38**, S449 (2005).

[22] B. C. Young, F. C. Cruz, W. M. Itano and J. C. Bergquist, 'Visible lasers with subhertz linewidths', Phys. Rev. Lett. **82**, 3799–3802 (1999).

[23] T. Kessler, C. Hagemann, C. Grebing, T. Legero, U. Sterr, F. Riehle, M. J. Martin, L. Chen and J. Ye, 'A sub-40-mHz-linewidth laser based on a silicon single-crystal optical cavity', Nature Photonics **6**, 687–692 (2012).

[24] J. D. Gillaspy, 'Highly charged ions', Journal of Physics B: Atomic, Molecular and Optical Physics **34**, R93 (2001).

[25] F. Currell, *The Physics of Multiply and Highly Charged Ions, Volume 1: sources, applications and fundamental processes*, 1st ed. (Springer Netherlands, 2003).

[26] J. C. Berengut, V. A. Dzuba and V. V. Flambaum, 'Enhanced laboratory sensitivity to variation of the fine-structure constant using highly charged ions', Phys. Rev. Lett. **105**, 120801 (2010).

[27] N.-H. Rehbehn, M. K. Rosner, H. Bekker, J. C. Berengut, P. O. Schmidt, S. A. King, P. Micke, M. F. Gu, R. Müller, A. Surzhykov and J. R. C. López-Urrutia, 'Sensitivity to new physics of isotope-shift studies using the coronal lines of highly charged calcium ions', Phys. Rev. A **103**, L040801 (2021).

[28] S. A. King, L. J. Spieß, P. Micke, A. Wilzewski, T. Leopold, E. Benkler, R. Lange, N. Huntemann, A. Surzhykov, V. A. Yerokhin, J. R. Crespo López-Urrutia and P. O. Schmidt, 'An optical atomic clock based on a highly charged ion', Nature **611**, 43–47 (2022).

[29] M. G. Kozlov, M. S. Safronova, J. R. Crespo López-Urrutia and P. O. Schmidt, 'Highly charged ions: optical clocks and applications in fundamental physics', Rev. Mod. Phys. **90**, 045005 (2018).

[30] F. Currell and G. Fussmann, 'Physics of electron beam ion traps and sources', IEEE Transactions on Plasma Science **33**, 1763–1777 (2005).

[31] M. Schwarz, O. O. Versolato, A. Windberger, F. R. Brunner, T. Ballance, S. N. Eberle, J. Ullrich, P. O. Schmidt, A. K. Hansen, A. D. Gingell, M. Drewsen and J. R. Crespo López-Urrutia, 'Cryogenic linear paul trap for cold highly charged ion experiments', Review of Scientific Instruments **83**, 083115 (2012).

[32] J. Stark et al., 'An ultralow-noise superconducting radio-frequency ion trap for frequency metrology with highly charged ions', Review of Scientific Instruments **92**, 083203 (2021).

[33] E. A. Dijck, C. Warnecke, M. Wehrheim, R. B. Henninger, J. Eff, K. Georgiou, A. Graf, S. Kokh, L. P. K. Sajith, C. Mayo, V. M. Schäfer, C. Volk, P. O. Schmidt, T. Pfeifer and J. R. C. López-Urrutia, *Cold highly charged ions in a radio-frequency trap with superconducting magnetic shielding*, accepted for publication in Review of Scientific Instruments. arXiv:2306.01670, 2023.

[34] P. O. Schmidt, T. Rosenband, C. Langer, W. M. Itano, J. C. Bergquist and D. J. Wineland, 'Spectroscopy using quantum logic', Science **309**, 749–752 (2005).

[35] P. Micke et al., 'The Heidelberg compact electron beam ion traps', Review of Scientific Instruments **89**, 063109 (2018).

[36] L. Schmöger et al., 'Coulomb crystallization of highly charged ions', Science **347**, 1233–1236 (2015).

[37] B. E. A. Saleh and M. C. Teich, *Fundamentals of Photonics*, 2nd ed., Wiley Series in Pure and Applied Optics (John Wiley & Sons, Ltd, 2007).

[38] P. D. Atherton, N. K. Reay, J. Ring and T. R. Hicks, 'Tunable Fabry-Perot Filters', Optical Engineering **20**, 206806 (1981).

[39] S. Wolff, A. Rodionov, V. Sherstobitov and H. Fouckhardt, 'Fourier-optical transverse mode selection in external-cavity broad-area lasers: experimental and numerical results', IEEE Journal of Quantum Electronics **39**, 448–458 (2003).

[40] H.-Y. Lo, J. Alonso, D. Kienzler, B. C. Keitch, L. E. de Clercq, V. Negnevitsky and J. P. Home, 'All-solid-state continuous-wave laser systems for ionization, cooling and quantum state manipulation of beryllium ions', Applied Physics B **114**, 17–25 (2014).

[41] C. Gohle, T. Udem, M. Herrmann, J. Rauschenberger, R. Holzwarth, H. A. Schuessler, F. Krausz and T. W. Hänsch, 'A frequency comb in the extreme ultraviolet', Nature **436**, 234–237 (2005).

[42] G. Berden, R. Peeters and G. Meijer, 'Cavity ring-down spectroscopy: experimental schemes and applications', International Reviews in Physical Chemistry **19**, 565–607 (2000).

[43] R. W. P. Drever, J. L. Hall, F. V. Kowalski, J. Hough, G. Ford, A. Munley and H. Ward, 'Laser phase and frequency stabilization using an optical resonator', Applied Physics B **31**, 97–105 (1983).

[44] A. Yariv, *Optical Electronics*, 4th ed., Holt, Rinehart and Winston Series in Electrical Engineering (Saunders College Publishing, 1991).

[45] R. V. Pound, 'Electronic frequency stabilization of microwave oscillators', Review of Scientific Instruments **17**, 490–505 (1946).

[46] E. D. Black, 'An introduction to Pound–Drever–Hall laser frequency stabilization', American Journal of Physics **69**, 79–87 (2001).

[47] K. Numata, A. Kemery and J. Camp, 'Thermal-noise limit in the frequency stabilization of lasers with rigid cavities', Phys. Rev. Lett. **93**, 250602 (2004).

[48] M. Abdel-Hafiz et al., *Guidelines for developing optical clocks with* 10^{-18} *fractional frequency uncertainty*, arXiv:1906.11495, 2019.

[49] P. F. Egan, J. A. Stone, J. H. Hendricks, J. E. Ricker, G. E. Scace and G. F. Strouse, 'Performance of a dual Fabry-Perot cavity refractometer', Opt. Lett. **40**, 3945–3948 (2015).

[50] S. Amairi, T. Legero, T. Kessler, U. Sterr, J. B. Wübbena, O. Mandel and P. O. Schmidt, 'Reducing the effect of thermal noise in optical cavities', Applied Physics B **113**, 233–242 (2013).

[51] SolidWorks render by N. Lackmann, 2023.

[52] T. Legero, email communication, 2022.

[53] T. Nazarova, F. Riehle and U. Sterr, 'Vibration-insensitive reference cavity for an ultra-narrow-linewidth laser', Applied Physics B **83**, 531–536 (2006).

[54] J. Keller, S. Ignatovich, S. A. Webster and T. E. Mehlstäubler, 'Simple vibration-insensitive cavity for laser stabilization at the 10^{-16} level', Applied Physics B **116**, 203–210 (2014).

[55] T. Ackemann, W. Grosse-Nobis and G. Lippi, 'The Gouy phase shift, the average phase lag of Fourier components of Hermite–Gaussian modes and their application to resonance conditions in optical cavities', Optics Communications **189**, 5–14 (2001).

[56] J. Morville, D. Romanini, M. Chenevier and A. Kachanov, 'Effects of laser phase noise on the injection of a high-finesse cavity', Appl. Opt. **41**, 6980–6990 (2002).

[57] T. Okoshi, K. Kikuchi and A. Nakayama, 'Novel method for high resolution measurement of laser output spectrum', Electronics letters **16**, 630–631 (1980).